# Breast phantom deformation tracking and local elastography for ultrasound-guided biopsy

M.N.M. (Marina) Castro

MSc Report

**Committee:**
Dr. F.J. Siepel
V. Groenhuis, MSc

July 2018

027RAM2018
Robotics and Mechatronics
EE-Math-CS
University of Twente
P.O. Box 217
7500 AE Enschede
The Netherlands

# Table of Contents


I. INTRODUCTION .......... 0

II. Underlying Concepts .......... 1

A. Breast Ultrasound .......... 1

1) Method of examination .......... 3

2) Color Doppler (CFM) .......... 3

3) Elastography .......... 4

4) Three-dimensional ultrasound .......... 4

5) Ultrasound-guided Biopsy .......... 4

B. Breast modeling .......... 5

1) Breast composition and development .......... 5

2) Breast deformation models and breast biomechanics 7

3) Tracking tumors for surgical assistance and biopsy11

III. Methods .......... 12

A. Preliminary studies .......... 12

1) Phantom fabrication .......... 12

2) Lesion and needle tracking in ultrasound videos . 14

B. Deformation tracking and elastography .......... 14

1) Gridpoints tracking algorithm .......... 14

2) Local deformation calculation algorithm .......... 18

3) Elastography .......... 19

IV. Results .......... 21

1) Phantom fabrication .......... 21

2) Deformation quantification .......... 22

3) Elastography .......... 23

V. Conclusions .......... 30

VI. Future Work .......... 30

Appendix .......... 31

References .......... 33

Thank You Note .......... 34

# Breast phantom deformation tracking and local elastography for ultrasound-guided biopsy

Marina Castro, RAM Intern, s2072319

*Abstract-* **This project's goal is to track deformations and calculate elastographic data using ultrasound imaging on phantoms with a fixed embedded referential.**

**Deformations caused by external pressure and needle insertion could be tracked and visually represented.**

**The proposed algorithms for elastography measurements show effectiveness in global terms but are locally less accurate. The algorithms were tested with homogeneous phantoms, but also using phantoms with heterogeneous compositions. For heterogeneous phantoms, different elastic properties can be perceived, but the Young's Moduli for the softer regions tend to be overestimated.**

*Index Terms*— **Breast biopsy, elastography, deformations, breast phantoms, image analysis, point tracking**

## I. Introduction

THIS report aims to sum up all the conclusions and work developed during the author's internship in the scope of MURAB project.

MURAB (MRI and Ultrasonic Robotic Assisted Biopsy) aims to improve precision and cost-effectiveness relation of breast biopsy for cancer diagnostic. This is to be done by the combination of Magnetic Resonance Imaging (MRI) and Ultrasound (US) Imaging, in order to reduce the usage of expensive MRI to the possible minimum and get even better results that the ones that this technique, alone, allows to. MRI allows for the precise and accurate detection of lesions but lacks real-time outputs, making the biopsy process time consuming, very dependent on the clinician proficiency and expensive. US imaging is already used for needle guidance during breast biopsy, and it allows for real-time needle guidance and for the patient to be in a more comfortable position and to undergo a faster and less traumatic biopsy procedure. Combining US imaging with the accuracy of MRI, whose produced image is registered with US image, and increased reproducibility, achieved by the introduction of robotics in this procedure (the US images are acquired by a fully automated robotic arm and the biopsy needle is positioned by a robot, too), presents a promising solution for the breast biopsy problematic.

Breast deformation needs to be considered in this problem's scope, since the position of the patient, and therefore the position of the breast, varies with the imaging method that is being used. Also, during the examination processes, the breast may be compressed and moved, making the study of displacements of its inner structures relevant to assure the accuracy of the biopsy: the displacements of the lesions need to be taken into account if one wants to accurately track them and remove samples during a biopsy procedure.

This being said, deformation quantization techniques must be developed. Deformations can be derived from elastographic data, if the applied pressures are known, or can be directly quantified, using reference points between which the deformations caused by certain forces are calculated. The latter technique, if applied through ultrasound imaging, could be useful for deformation quantization in the scope of Ultrasound Guided Biopsy and MURAB project – **calculating both deformations and elastographic data using an algorithm that processes Ultrasound Imaging is the research question that this project aims to answer to.**

With the latter principle in mind, the goal of this internship project was to create a referential system inside a breast phantom, track the deformations of this referential grid using US imaging and even estimate the elastic properties of the phantom, since both the displacements and applied pressures can be measured.

This method could be used as a starting point for estimation of deformations in phantoms with increasing complexity, and also as a reference for the development of other methods for deformation tracking and elastic properties estimation.

The ultimate goal may concern not only deformations in the breast caused by external surface pressure, but also by needle insertion, since the aim can be extended to the achievement of real-time correct needle positioning. The approach is to create a grid of ultrasound echogenic lines inside an anechoic breast phantom, which creates an internal referential for needle movement and deformation tracking. An automatic image processing algorithm is optimized to quantify the deformations in 2D.

Because breast tissue is not homogeneous, the project includes the simulation of different layers and inclusions in breast tissue via the creation of breast phantoms with heterogeneous constitutions.

This report is divided in sections and subsections. Section II will present a deep insight on the underlying concepts used, not only to prepare this project in specific, but to understand the whole scope of MURAB project and some of the areas one can dive in while researching on ways to make this novel assisted biopsy technique possible. Not all of the Underlying Concepts presented can be directly applied to the author's project.

Section III presents the methodologies for the development of the algorithm used for deformation tracking and elastography measurements, but also other important techniques, such as the creation of phantoms designed in an optimized way for this specific project.

Section IV presents the results acquired in this project, going from the created phantoms, to the deformation measurements, to elastography results through different methods.

Section V refers to the conclusions of this project, being followed by a section on the insights about possible future work that can be done in this scope.

## II. Underlying Concepts

So as to present a deeper insight on the topics that correlate with this section of the MURAB project and this internship project, in specific, some relevant concepts will be explained in the subtopics of this section: the breast ultrasound imaging technique, since this is the technique used for visualization of the referential grid built for deformation tracking, needle guidance via ultrasound for biopsy procedures, and some subjects used to build the physical and mathematical foundations of the proposed method.

In subsection A, one may acquire broad knowledge on the breast ultrasound thematic: its physical principles, its comparison to other imaging techniques, the advice on when it should or should not be used, and its advantages and disadvantages. Also, the method of examination using this methodology is explained, with not as much detail as would be necessary in clinical practice, but sufficient to acknowledge the problematics involved in it. Some additional technology modules that can provide information to be combined with breast ultrasound methodologies, such as color Doppler, Elastography and 3D breast ultrasound are introduced in this section, and its utility is discussed. For 3D breast ultrasound clarification, an experiment with axillary metastases and the author's visualization of an experiment the internship's context are cited. Then, ultrasound guided biopsy is contextualized.

In section B, breast modeling techniques are detailed, after a brief introduction on why they are necessary, how does breast ultrasound interfere in the subject and how they are processed. The most common method of breast modeling, Finite Element Model (FEM) is presented and a basic-level explanation on its computation and use is detailed.

Breast composition and development through a lifetime are mentioned, starting with why those are relevant for the context. General anatomy of the breast in illustrative examples and visualized via breast ultrasound are considered.

Breast deformation models and breast biomechanics play one of the most relevant roles in the whole scope of the MURAB projects, so the approach followed to address to them was the overview of four studies.

The Underlying Concepts section ends with a small section on tracking tumors for surgical assistance and biopsy. The problem is explained and contextualized through a study on the subject. Due to the lack of literature on this matter, the problem of needle insertion is addressed in this section, through a paper overview, but not detailed in the scope of ultrasound guided biopsy.

### *A. Breast Ultrasound*

Established as one of the three main techniques for imaging diagnostics of the breast, together with magnetic resonance imaging (MRI) and mammography, the breast ultrasound itself, or its combination with the referred modalities, is used for early detection of breast cancer, owning advantage in dense breasts (especially in premenopausal women) and being able to provide additional information when dealing with lesions that cannot be fully classified by MRI and mammography alone.

According to [1], sonography is more sensitive in the examination of invasive carcinoma in X-ray dense breasts than mammography. Ultrasound has also the advantages of not using ionizing radiation (which mammography does) and corresponding better to the real anatomy of the breast than mammography results. As for MRI, it is known that its sensitivity is superior to that of the other two methods, even though its methodical performance remains to be standardized [2].

Ultrasound is considered, in addition to mammography, in cases of high-risk women for whom magnetic resonance imaging (MRI) screening may be appropriate but cannot have MRI for any reason or in women with dense breast tissue, according to [3]. It is also indicated for diagnostic clarification of the symptomatic breast (palpatory findings, pain), sonographic localization of lesions detected by MRI, post-treatment care and monitoring of tumor reactions during primary chemotherapy. [4]

Several published papers have reported that breast ultrasound screening in women with dense breasts and negative mammograms on clinical examinations yielded an increased cancer detection rate of 2.8 to 4.6 cancers per 1,000 women [3]. Breast density itself is an independent risk factor for the development of breast cancer (although controversial): the relative risk of breast cancer for women with the densest breasts is two to six times larger than that of women with the least dense breasts. Breast ultrasound is, then, a fundamental imaging technique for the cited cases.

The group that experimented with breast density parameters in breast ultrasound, [5], plotted the relation expressed in **figure 2,** between the sensitivity of mammography or breast sonography and breast density, according to the ACR category, which classifies the breasts according to their density (proportion of glandular tissue) in numbers ranging from 1 to 4, to which corresponds an increasing proportion of glandular tissue, from 0 to 100%. The conversion to ACR category is shown in **figure 1.**

| ACR | Proportion of glandular tissue (%) |
|---|---|
| 1 | 0-24 |
| 2 | 25-50 |
| 3 | 51-75 |
| 4 | 76-100 |

*Figure 1-ACR (American College of Radiology) categories of breast density [4]*

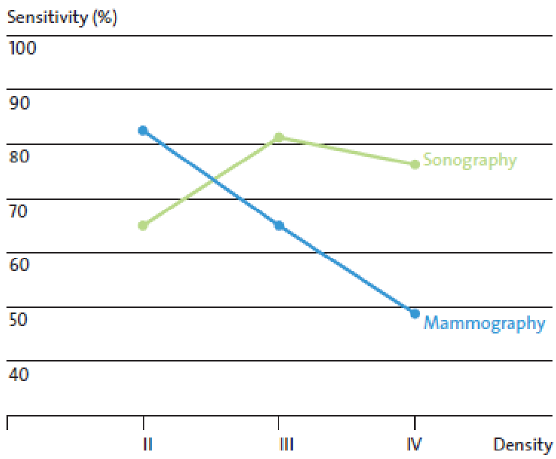


*Figure 2- sensitivity of mammography and breast sonography dependent on breast density according to ACR category (based on the studies of [5], taken from [4]*

In [6], a study that states that sonography is the leading method in diagnostics of symptomatic alterations of the breast is presented. With the aid of breast ultrasound, it is possible to precisely recognize diffuse benign (fibrocystic, mastopathic) alterations of the parenchyma and benign lesions, most of which can be conclusively categorized. The sensitivity of mammography and sonography in symptomatic patients from different age groups is plotted in the **figure 3.** The same team [6] tried to establish a correlation between the choice of initial breast imaging examination with the woman's age, arriving to the conclusion that sensitivity and specificity of each test were not linearly associated with age. However, the sensitivity of mammography increased substantially in women older than 50 years, and in women 45 years old and younger, the sensitivity of sonography was 13,2% greater than that of mammography.

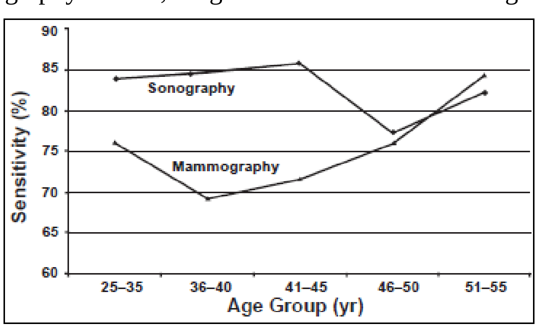


*Figure 3 – sensitivity of sonography and mammography in symptomatic patients from different age groups*

Despite the referred advantages of breast ultrasound, screening ultrasound studies have reported high false-positive rates, low reproducibility, low positive predictive value for biopsy recommendations, operator dependency of the examination, inability to image most DCIS (ductal carcinoma in situ) cases, and lack of agreement on which solid or complex lesions found at screening require biopsy, conferring to the technique its utility only as a supplemental screening method, combined with mammography or MRI [3]. Also, breast ultrasound use can be greatly limited if the breasts are too large and mobile, making it difficult to scan thoroughly, or in post injury, surgery or biopsy scenarios, in which the resultant hematoma will reduce detail and may obscure pathology.

Breast ultrasound techniques are not only used for screening, but also for biopsy guidance – aspiration or biopsy procedures of lesions seen only on sonography (and others) can be readily performed [7].

Even though there are multiple variants of the breast ultrasound methodology, which provide different or additional information, its basic principles rely on the reflection of acoustic waves from interfaces of varying impedance [4]. Ultrasounds are characterized as sound waves with frequencies above 20 kHz, whose pulse travels to the target tissues and is reflected in every interface. A transducer can calculate the distance between itself and a reflection point through the time it took the wave to be generated and then reflected, arriving to the detector. The sound waves do not only reflect when they reach an interface – they are diffracted, a phenomenon that depends on the wavelength and on the media. The speed of the wave propagation is proportional to the density of the tissue, given the property of acoustic impedance of each tissue, which translates the resistance of the tissue to the movement of a sound wave.

Given this, the image provided by the breast ultrasound methodology can give rise to multiple parameters that can classify a finding: its localization, size, form, axis, border, echogenic margin (which may or not be present), echogenicity, wave transmission (acoustic shadowing, indifferent, enhanced, and mixed), calcification and alterations in surrounding tissue. Echogenicity is an important concept in ultrasound imaging, translating the tissue's ability to return the signal, higher when the surface reflects increased sound waves. Tissues that have higher echogenicity are called "hyperechogenic" and are usually represented with lighter colors on images in medical ultrasonography. In contrast, tissues with lower echogenicity are called "hypoechogenic" and are usually represented with darker colors. Areas that lack echogenicity are called "anechogenic" and are usually displayed as completely dark [4].

Other parameters can arise from additional technological modules in breast ultrasound such as compressibility, relocatability, 3D criteria and circulation (and quantity of vessels) [4].

The breast ultrasound methodology is dependent on the user proficiency and on the quality of the equipment. The price of the equipment may rise from 40,000 to 60,000 Euros and must be equipped with high frequency linear transducer probes (with a bandwidth between 5 and 15 MHz – a lower frequency transducer may be required for the larger attenuative breasts, inflammatory masses and the axilla). Besides the transducers, also the signal processing performance of the hardware is of relevance and the integration of a color Doppler is nowadays broadly considered, given the important additional information for breast lesion characterization that it can provide (in terms of verification of vascularization) [4].

*1) Method of examination*

According to [4], sonographic examination of the breast is carried out with the patient lying down, supine, with arms elevated. The examination is done on the transverse and longitudinal planes of the breast, as there might me a risk of incomplete examination. A radial examination technique may be also used to examine the central retromammillary efferent and peripheral milk ducts in the longitudinal plane. The main axillae structures should also be examined for alterations to the lymph glands. The **image 4**, taken from [4] illustrates the recommended path of the probe.

*2) Color Doppler (CFM)*

As stated previously, there are many additional technological modules in breast ultrasound. One of them is color Doppler, CFM, which can be used to color code erythrocyte movement in tumor vascularization.

It is known that malign tumors induce angiogenesis in order to make their uncontrolled growth possible. Therefore, using this technique, differentiation is made between evidence of vascularization or non-vascularization, and one can observe and conclude on the pattern of circulation.

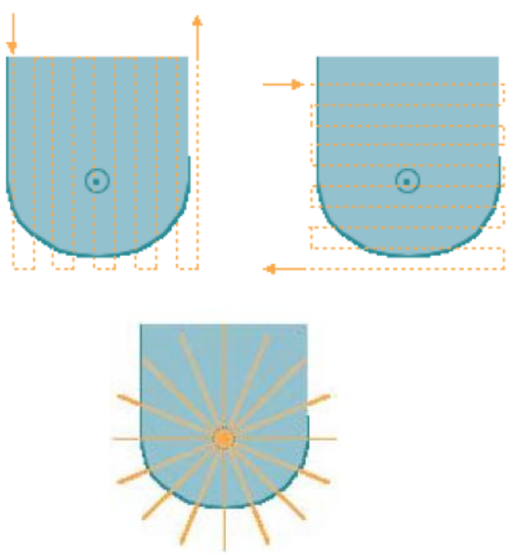

*Figure 4 – the first two images represent the meandering path of the transducer probe on two planes and the third the radial path of the transducer probe for imaging the efferent and milk ducts on a longitudinal plane*

Almost all the criteria for characterizing a breast lesion with the aid of color Doppler can be found in [8]:

- Vessels in marginal areas of lesions are more likely to be non-suspect;
- Vessels with a radial pathway and vessels with higher and varying speeds, also spiral vessel pathways, are typical of malignoma;
- Aggressive, highly malignant carcinoma show earlier and more distinct flow signals;
- There may not be any sonographically detectable flow signals in malignant lesions, but they may, on the other hand, be found in benign findings (like myoxoid fibroadenoma and lactating adenoma).

Color Doppler imaging may help differentiating between malignant and benign solid breast masses, but it does not show high predictive values, so its role is only complementary to the high-sensitive B-mode (brightness mode) evaluation raising or confirming the doubts upon indeterminate or suspicious lesions.

MRI is significantly better when considering vascular items, but intra-tumoral blood-flow analysis by color Doppler ultrasonography correlates well with histological grade and aggressiveness of the cancer, being suitable for use as a first step assessment of the efficacy of neoadjuvant and antiangiogenetic treatments. [8]

An example on how this technique can be useful on the detection of carcinomas is presented on the **figure 5.**

*Figure 5 – taken from [4]; the upper image shows a smooth bordered, hypoechoic homogeneous tumor (suspected protein-containing cyst or fibroadenoma). Its sole observation in B-mode (brightness mode) classifies the tumor as probably benign (BI-RADS3); the second image shows the same finding in color Doppler: very strong hypervascularization, increasing the rank of the finding to a BI-RADS4, which denotes a suspicious lesion, for which core needle biopsy is recommended*

### 3) Elastography

As described in [4], elastography is implemented by some manufacturers as a procedure by which the elastic characteristics of the scanned tissue are displayed with a color code. The structures of carcinomas and those of more elastic tissue with benign alterations can be easily distinguished through this technique.

This modality is used as a complement for the breast ultrasound B-mode, as it introduces additional specificity.

There might be overlapping in the elasticity characteristics of benign and malignant tumors, making the elastography procedure results depend on the user and lack reproducibility.

The output images of elastography over B-mode ultrasound can be seen on **figure 6.**

### 4) Three-dimensional ultrasound

As described in [9], the three-dimensional ultrasound imaging technique aims to overcome the limitations of the conventional two-dimensional breast ultrasound, in which the clinician has to mentally transform a sequence of 2D images into a three-dimensional tissue structure in order to make a diagnosis. This demands considerable skill of the clinician and inevitably leads to inaccuracies in assessing morphological features, sizes and staging of lesions, and in monitoring subtle changes. Moreover, a 2D image location is often difficult to reproduce in sequential examinations, impeding quantitative serial studies.

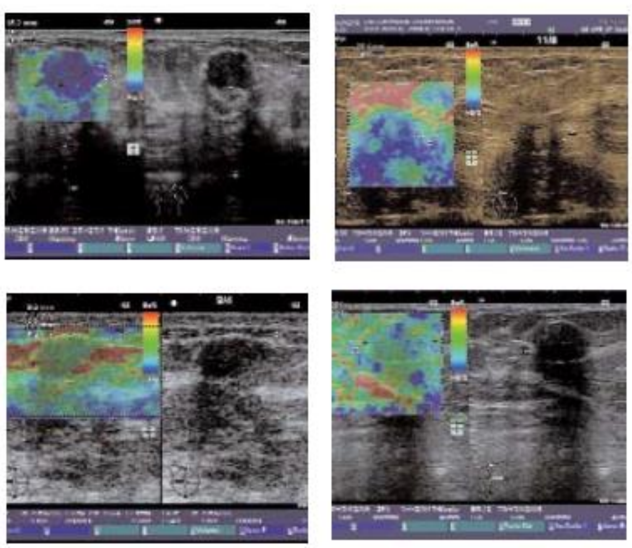

*Figure 6 – The upper images represent a carcinoma, in blue, while the two images below represent a fibroadenoma (brown-red or green) in elastography. A carcinoma is a malignant tumor that arises from glandular epithelial cells, while a fibroadenoma is a benign breast condition characterized by the proliferation of stromal and glandular elements. Using elastography, these two conditions can be distinguished easily.*

The existent 3D ultrasound imaging technology, back in the year of the writing of [9], used conventional 2D images to construct a 3D data set. The acquisition of 2D images could be mechanical, with the ultrasound probe moved by a motor in a predefined manner, or free-hand, in which the clinician holds the probe and manipulates it freely over the anatomical structure to be examined. In free-hand acquisition, a localizer is required to record the position and orientation of each 2D scan in order to reconstruct the 3D anatomy.

The combination of the sweeps, which create 2D images, is called spatial compounding, which helps reduce speckle noise when sweeps are taken along different directions. The soft nature of the breast causes the problem of easy deformation, which differs for each scan acquired. For each sweep, even under careful scanning, the anatomy inside the breast undergoes small deformation. This thematic will be detailed later in this overview.

### 5) Ultrasound-guided Biopsy

An experiment to evaluate the accuracy of ultrasonography alone and in combination with fine-needle biopsy (FNAB) for detection of axillary metastases of nonpalpable lymph nodes in breast cancer patients was conducted by the team of Jorien Bonnema, whose results are displayed in [10].

Ultrasound-guided FNAB had a sensitivity of 80% and a specificity of 100% and detected metastases in 63% of node-positive patients.

For the study, and also as a common practice, the team used a 21-gauge needle to extract by aspiration the nodes in the axillae, making then an analysis of the aspiration biopsies in which cytological features that could classify the specimen as malignant or benign were looked for. The axillary specimens are processed for histological examination using hematoxylin and eosin (H&E) and examined by a pathologist.

This experiment presents the many advantages of the ultrasound-guided biopsy, such as its little invasiveness (compared to surgical biopsy) and little or no scar formation.

The biopsy procedure can be conducted by fine needle aspiration (FNA), which uses a very small needle to extract fluid or cells from the abnormal are, which is the case, but also by core needle (CN), which uses a large hollowed needle to remove one sample of breast tissue per insertion, vacuum-assisted device (VAD), which uses a vacuum powered instrument to collect multiple tissue samples during one needle insertion and wire localization, in which a guide wire is placed into the suspicious area to help the surgeon locate the lesion for surgical biopsy.

With continuous ultrasound image, the physician is able to view the biopsy needle or wire as it advances to the location of the lesion in real-time.

This procedure can easily be exemplified with the ultrasound images collected in the context of the review's author internship in the MURAB project. Examples of these are the images on the **figure 7,** in which a breast phantom ultrasound image can be seen, and the lesion inside it located through its hypoechogenic appearance. The needle is inserted into the phantom and tracked all the way through the simulated tissue to the simulated lesion, creating an hyperechogenic region, corresponding to the needle itself. According to the properties of the needle, it can generate possible artifacts such as shadowing. Because of this, a special coating for the biopsy needles can be applied.

### B. *Breast modeling*

When the purpose is to have ultrasound guided biopsy and even the combination of imaging techniques for breast cancer screening, as in the context of the MURAB project, creating models of the breast, either physical or digital, is of uttermost relevance.

Computational models can be used to simulate the deformations caused by external forces, the imaging processes or needle insertion, and, to do that, one must estimate the elastic properties of the breast and apply them in the said models. Surface segmentation, rigid registration and finite element analysis and modeling are keywords in the process. The deformations applied in the breast can be modeled by affine and elastic transformations, e. g.

Under the context of ultrasound imaging, the deformation of the breast due to gravity load, since the patient is lying down, supine, with the arms elevated, needs to be simulated. This simulation may concern the breast shape change due to transitioning from prone to supine position or from standing position to supine position.

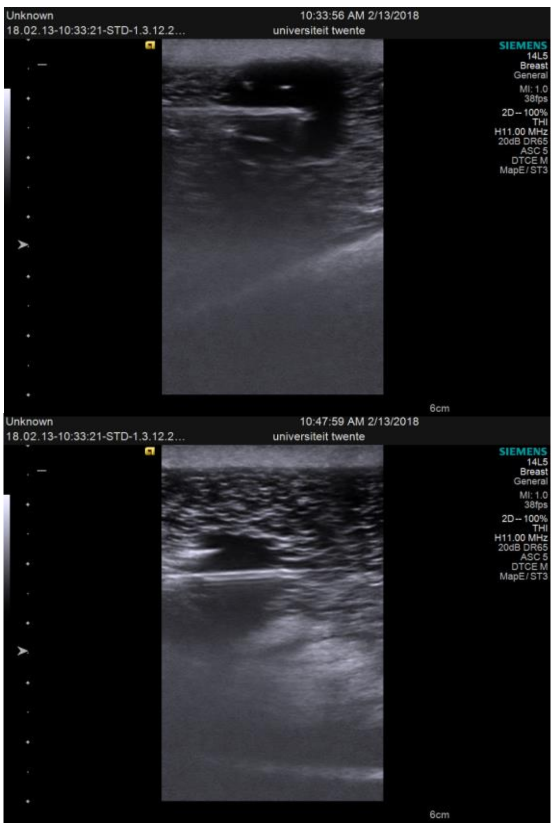


*Figure 7 – Ultrasound-guided biopsy images: in the first image, one can see the darkened breast lesion and the lighter, horizontal needle coming from the left; in the second image, the needle is made of a more reflective material, creating shadowing in the bottom of the lesion, making it lighter*

The physics based numerical procedures presented by [11] for biomechanical modeling and soft tissue deformation may be either based on linear or nonlinear biomechanical models, such as the mass-spring method (MSM), mass-tensor method, boundary element method and conventional finite element method (FEM). In MSM, an object is modelled by a collection of point masses linked together with massless springs. On the other hand, FEM subdivides a body into a set of finite elements (tetrahedral, hexahedral in 3D or triangles and other 2D polygons) and the displacements and positions of each element are approximated from discrete nodal values using interpolation functions. There are different choices for the element type, as said, but also for interpolation functions, whose choice depends on the accuracy requirements, geometry of the objects and computational complexity. Also, the accuracy of the calculations made on the FEM depends on the number of elements that we choose to have in the mesh to represent the complex object: the breast. The higher the number of elements, the higher the accuracy of the calculations, the smaller the size of the elements, and, therefore, the higher the number of necessary calculations – there is an increase in computational cost.

In FEM, so that we know what happens when a given force is applied to a certain region of the object, we need to describe mathematically an equation for the whole system. A displacement equation is defined for each node of each element, so that each element is defined by a matrix with as many equations as nodes. This matrix is the base for a series of steps based on the fundamental laws of mechanics, that go from relating displacements and stresses to getting the strain energy from those stresses and finally derive the potential energy. As an analogy with the equation for the behavior of a simple string, the matrix with the node equations is named the stiffness matrix of the element. Combining the stiffness matrixes of all the elements in one, one can get the matrix that represents the stiffness of the system as a whole.

Two neighboring elements have common nodes, condition that creates some value repetitions in different matrixes, for different elements. This given, the combination of element stiffness matrix cannot be done through a simple merging technique: to solve the whole system of equations (to have the stresses, starting from all the nodes in all the elements), all the stiffness matrixes are combined through the process of reduction. In the process of reduction, part of the matrix is eliminated so that the matrix lines correspond to sets of simultaneous equations. Then, the equations are progressively solved, and the values replaced in the following ones, so that when the last matrix is added, a solution for one only node is obtained. Then, the result for this node is used as a "key", backpropagating to the previous equations of the system until the displacement for every node is obtained. From these results, one can calculate the corresponding stresses.

The generation of a FEM is done using a dataset of radiological 3D images of the anatomy of the breast and then classifying and segmenting the tissue. These steps are followed by tissue surface reconstruction, FEM volumetric mesh generation and tissue type assignment for the FEM mesh.

#### 1) *Breast composition and development*

Breast modeling cannot be fully conquered without a precise insight on the histological constitution of the breast, since the properties of the gland vary depending on the tissue type and the breast is characterized by great heterogeneity.

Also, the breast is not a static gland. Its mutations and evolution throughout a women's life need to be considered to apply the right tissue properties to a model, given by the different constitutions that can be possible during the process of puberty, lactation, menopause and aging.

The breast anatomy and development can be fully comprehended through the work of [12]. It enhances that understanding the breast anatomy is an important adjunct to a meticulous clinical breast examination, as it is for breast modeling. A more clinical approach on breast anatomy can be found in [13].

The female breast lies on the anterior thoracic wall. Its base extends from the second to the sixth rib. The epidermis of the nipple and areola is pigmented and wrinkled, and the skin of the nipple contains numerous sebaceous and apocrine sweat glands and little hair. The 15 to 25 milk ducts (see **images 11 and 12**) enter the base of the nipple, where they dilate and form the milk sinuses. The circular areola surrounds the nipple and varies between 15 and 60 mm in diameter. Its skin contains hair, sweat glands, sebaceous glands, and Montgomery's glands, which are large, modified sebaceous glands with miniature milk ducts that open into Morgagni's tubercles in the epidermis of the areola.

Deep in the areola and nipple, bundles of smooth muscle fibers are arranged radially and circularly in the dense connective tissue and longitudinally along the lactiferous ducts that extend up into the nipple. These muscle fibers are responsible for the contraction of the areola, nipple erection, and emptying of the milk sinuses.

The mammary tissue extends variably into the axilla as the glandular Tail of Spence. The posterior surface of the breast rests on portions of the following muscles: fasciae of the pectoralis major, serratus anterior, external abdominal oblique, and rectus abdominis muscles. [13]. On **figure 8,** one can see the fascial system of the breast, including the ligaments of Cooper, fibrous and elastic prolongations that divide the gland into multiple septa and give suspensory support to the breast.

On **figure 10,** the normal ultrasound breast anatomy can be seen. The ultrasound breast anatomy of a lactating breast can be observed on **figure 11.**

On **figure 9,** one can see an overall view of the chest and inclusion of breasts, as well as the main anatomical features that can correlate to breast function.

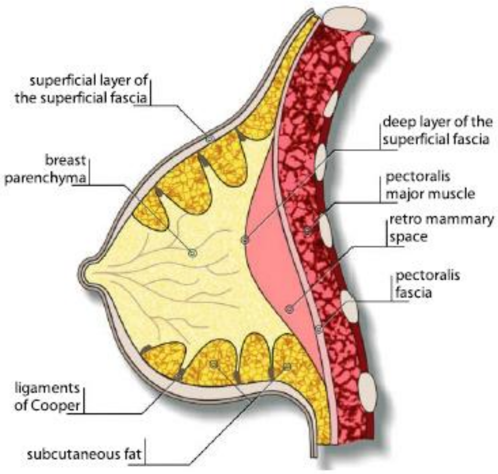


*Figure 8 – Fascial system of the breast [13]*

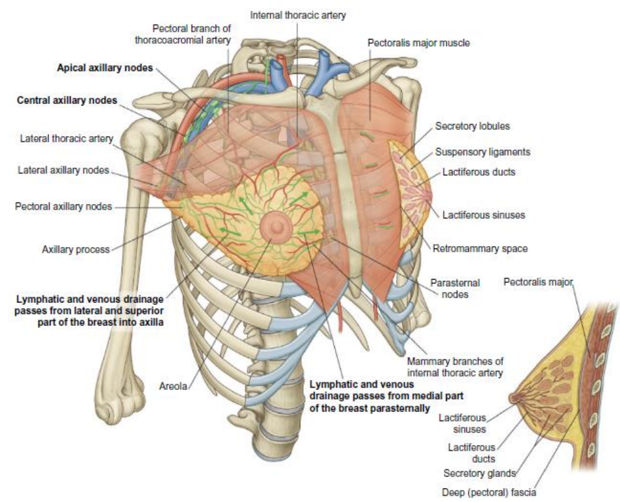


*Figure 9 – the anatomy of the breast and surrounding anatomical structure, taken from [14]*

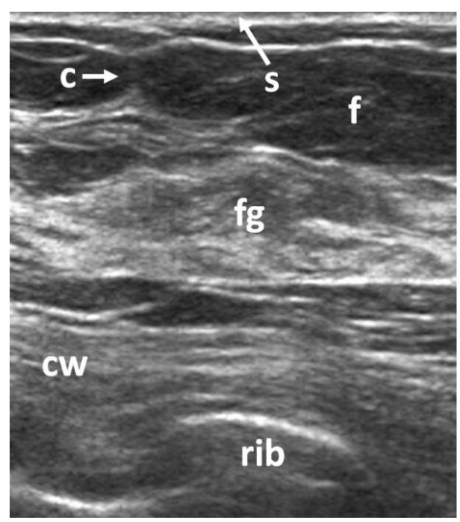


*Figure 10 – normal ultrasound breast anatomy. The breast is covered by hyperechoic skin (s). Within the breast is fat (f) and a variable amount of fibroglandular breast tissue (fg), all positioned over the chest wall (cw), with visible ribs. Note that Cooper ligaments (c) are visible as they connect to fascia and skin (s). [15]*

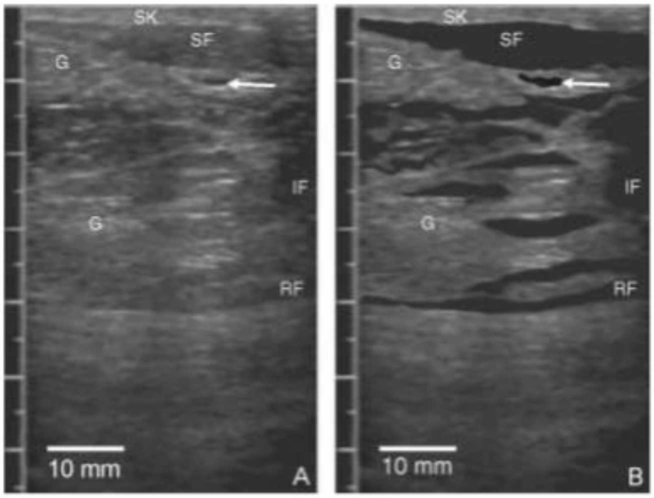


*Figure 11 - (A) Ultrasound image of tissues of the lactating breast. (B) The skin (SK) is shown as an echogenic (bright) line at the top of the image. The subcutaneous fat (SF) is less echogenic and situated below the skin. The intraglandular fat (IF) is of similar echogenicity to the subcutaneous fat. The glandular tissue is echogenic (G) while the milk duct (arrow) appears as a hypoechoic tubular structure. The retromammary fat (RF) is a thin hypoechoic band along the chest wall. [16]*

The embryology of the breast [12] is important to understand the role of each tissue in it and the development of the breast throughout a women's lifetime: mammary glands are a modified and highly specialized type of sweat gland. Only the main lactiferous ducts (see **figure 12**) are formed at birth, and the mammary glands remain underdeveloped until puberty. At that point, the breast enlarges under the influence of ovarian estrogen and progesterone production leading to proliferation of epithelial and connective tissue elements. Also at puberty, the breast enlarges due to the development of the mammary glands and increased deposition of fatty tissue. Only during the onset of pregnancy, the breast completes its development. At this time, the breast enlarges with increases in volume and density, the superficial veins dilate, and the nipple areola complex darkens. During the first trimester of pregnancy, the stromal elements of the breast are gradually replaced by the proliferating glandular epithelium and during the third trimester, the epithelium differentiation results into the development of secretory cells that are able to synthesize and secrete milk proteins. Oxytocin induces myoepithelial proliferation and differentiation. After delivery, prolactin, along with growth hormone and insulin, induce production and secretion of milk. In response to neural reflexes activated by suckling, oxytocin regulates the secretion of milk.

Involution occurs when lactation is not performed anymore and the glandular, ductal, and stromal elements atrophy resulting in decrease in breast size.

The breast anatomy changes during menopause and its modifications need to be considered in order to create precise models. The breast regresses and the ductal and glandular elements involute resulting in the breast predominantly containing fat and stroma. With aging, there is an overall reduction in the number of ducts and lobules. Over time, fat and stromal elements decrease, resulting in breast shrinkage and loss of contour. The suspensory ligaments of Cooper relax with time and eventually result in breast ptosis.

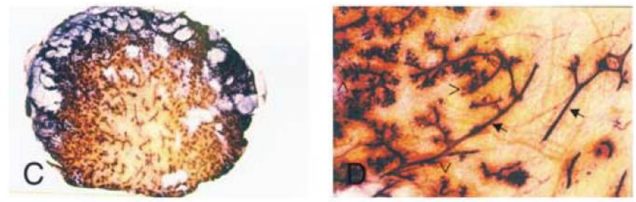


*Figure 12 – C is a carmine-stained whole-mount preparation of the breast of a 15-year-old female. This is a coronal section X0.5. D is a higher power view of the area of C. Arrows indicate ducts and unfilled arrowheads indicate ductal termini (X2.5) [17]*

*2) Breast deformation models and breast biomechanics*

In the study presented in [18], it is stated that affine transformations are used to model the global motion of the breast and local breast deformations are modeled by free-form deformations (FFD) based on B-spline. A B-spline, or basis spline, is a spline function (piecewise polynomial parametric curve) that has minimal support with respect to a given degree, smoothness, and domain partition.

The same study uses the approach of creating a regularization term (since their problem is related to the deformations caused by image registration) that is a local volume-preservation (incompressibility) constraint, motivated by the assumption that soft tissue is incompressible for small deformations and short time periods. This means that the tissue can be deformed locally, but, like a gelatin-filled balloon, the volume (local and total) remains approximately constant. The incompressibility constraint is implemented by penalizing deviations of the Jacobian determinant of the deformation from unity.

To avoid volume loss in the modeling problem (in the cited study, when doing non-rigid registration of contrast-enhanced images), one may couple the control points of a free-form (B-spline) deformation in order to make a portion of the object (in their case, the contrast-enhancing lesion) locally rigid. The approach requires identification of the rigid structures and makes the structures compulsorily rigid, even in cases where they actually have to be deformed.

Prior to this study is the one described in [19] that aims to model breast deformation concerning its complex anatomy (due to the different types of interwoven breast tissue whose properties are distinct) for the purpose of generating synthetic mammograms. They approximate breast compression by separate deformations of tissue layers positioned normal to the compression plates. The 3D mammography they aim to create can also serve as a complement to experiments with respect to positioning, compression and acquisition.

This team creates a whole set for mammography simulation, which contains, other than the x-ray image acquisition model, a 3D software breast phantom and a compression model.

The breast phantom is a software tissue model that contains two ellipsoidal regions of large scale tissue elements: predominantly adipose tissue and predominantly fibroglandular tissue. The internal tissue structures of these regions, such as the adipose compartments and the breast ductal network, are approximated by realistically distributed medium scale phantom elements, such as shells, blobs, and the simulated ductal tree. The anatomic structures of the breast included in the tissue model can be seen in the **figure 13**.

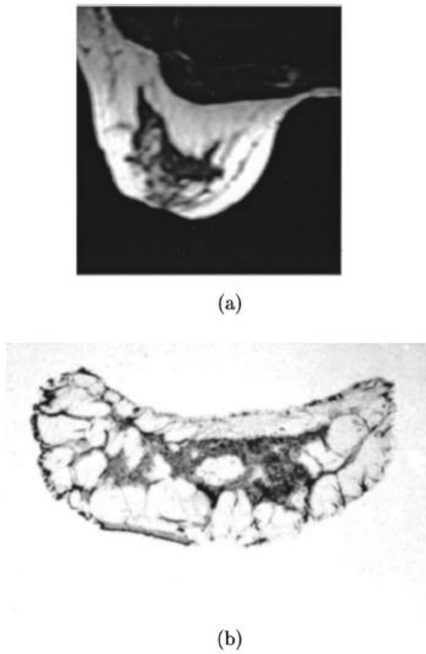


*Figure 13 – anatomic structures of the breast included in the tissue model proposed on [19]. (a) presents the large scale regions seen in MRI images as predominantly adipose tissue (bright region). (b) is a thick histologic slice showing large scale regions of adipose tissue and fibroglandular tissue and medium scale tissue structures: compartments surrounded by Cooper's ligaments in the adipose tissue and small adipose cavities and ducts within the fibroglandular tissue*

The compression model is based upon tissue elasticity properties and a breast deformation model. As deformation is simulated separately for tissue layers, which are positioned normal to the compression plates (necessary to the mammography procedure) the model for the compressed breast is a stack of deformed slices.

The team modeled the adipose tissue compartments approximating them by thin shells in the adipose tissue region and small blobs in the fibroglandular tissue. The interiors of the shells and blobs have the elastic and x-ray attenuation properties of adipose tissue, since the main goal of the simulation is its use in x-ray imaging. The adipose compartments were firstly approximated by spheres of various sizes, which would vary to allow for normal breast anatomic variations.

On **figure 14**, one can see in detail the orthogonal cross-sections of the breast tissue phantom. There are simulated regions of predominantly adipose and predominantly fibroglandular tissue, together with the spherical approximation of adipose compartments in those regions. The size of these compartments differs for adipose and fibroglandular tissue. On **figure 15,** the different sized adipose compartments are illustrated.

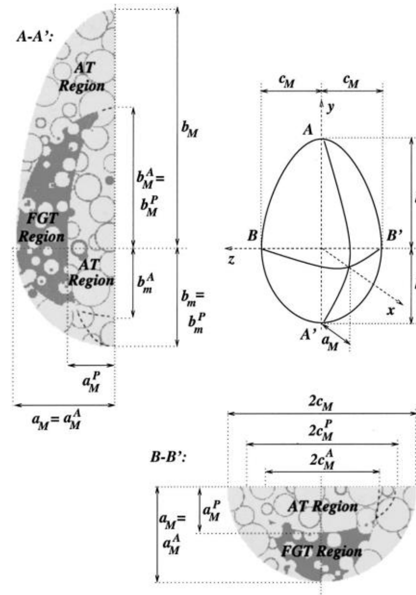


*Figure 14 – orthogonal sections of the uncompressed breast model. Parameters without subscripts correspond to the semi-axes of the ellipsoidal approximation of the breast outline; superscripts A and P correspond to the anterior and posterior border of the fibroglandular tissue model region, respectively*

The team also modeled the breast ductal network. They focused on the pattern of duct branching, which can be expressed by a ramification matrix, representing probabilities of branching at different levels of a tree structure. The least constrained branching pattern was acquired with a class of random binary trees. The ductal model consists of 15 lobes, each one simulated by a different random binary tree. Different trees are generated by using different random number generator seeds. A representation of the network is shown in **figure 16.**

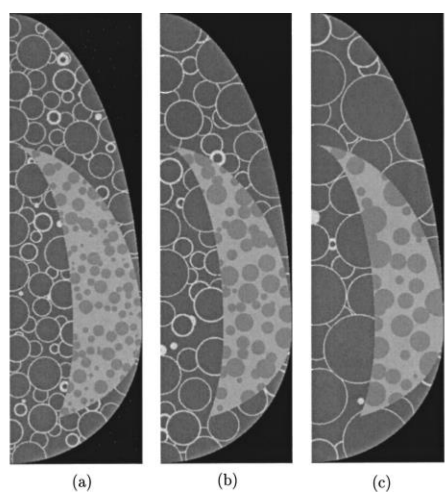


*Figure 15 – sections of breast models with different sized tissue elements*

Another part of this team’s study consisted on modeling the mammographic compression model, which was based upon a deformation model including realistic tissue elasticity properties. Because the experiments for determining the elastic properties of the breast tissues are conducted using small samples taken from a particular tissue type, elasticity parameters of the tissues found on literatures vary significantly.

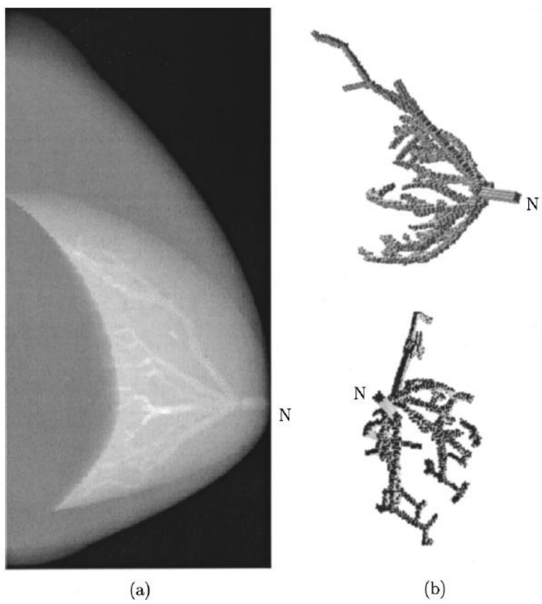


*Figure 16 – examples of computer generated local lobes. In a, one can see a simulated mammogram with five duct lobes. In b, two views of the same simulated ductal network, used to generate the image in a, are seen. The letter N indicates the position of the nipple*

The considered parameters for elastic properties are the Young’s modulus, E, and the Poisson’s ratio, ν. The Young’s modulus relates the strain, measure of deformation as the fractional change in length, to the stress (force applied to the surface area of the deformed object). The Poisson ratio is given by the ratio of transverse contraction and elongation of a deformed bar. As it is usually assumed that human tissue can be approximated as an incompressible material, those volume does not change during deformation, these properties are adapted to the study. For incompressible materials, ν is approximately 0.5.

The other elasticity moduli used to describe the behavior of material are the bulk modulus, K, and shear modulus, G, which can be expressed using the values of E and ν:

$$K = \frac{E}{3(1-2\nu)}, G = \frac{E}{2(1+\nu)}.$$

The elastic parameters of the tissues were acquired by the team through the following method: knowing that there is a relationship between the bulk elasticity modulus, K, material density, ρ, and the speed of sound through the material, v, given by:

$$\mathrm{v} \approx \sqrt{\frac{K}{\rho}}$$

the parameters could be computed using the values of ultrasound velocity through various tissues found in the literature.

Furthermore, the team’s experiments in creating the compression model are not applicable in contexts outside of mammography, since they include the compression of the breast between plates, which does not happen, e. g., in breast ultrasound, where the modeled applied force should be the gravitational, given the supine position of the body. Nevertheless, without getting in detail, it is explained that, in the team’s compression model, tissue deformation is estimated in two phases: first, the large scale model elements of adipose and fibroglandular tissue regions are deformed to determine the shape of the compressed breast; second, the medium scale model elements are deformed by transforming the shells and spheres into ellipsoids. Given the sliced nature of the simulation, deformation of each slice is computed in three steps: first, a rectangular slice approximation is computed; second, slice deformations are estimated using a composite beam model; third, the compressed slice shape is computed from the deformed rectangular approximation. Compressed slices are stacked together to form the compressed breast model shape.

An approach that is directly correlated with breast ultrasound is the one followed by [9]. The goal of the team was to perform nonrigid registration of 3D free-hand ultrasound images of the breast, but they encountered with the problem of substantial deformation of the breast during scanning, which often causes misregistration in spatial compounding of multiple scan sweeps. However, to overcome the problem, the team used image processing techniques.

The approaches in this problem vary, and the one explained in [20] uses the already explained FEM to predict mechanical deformations under external perturbations. This article dives precisely into the problem of live guidance during needle breast procedures, with the creation of a virtual reality system for guiding breast biopsy with MR imaging, which uses a deformable finite element model of the breast. On section III-C, more examples on this thematic are presented.

The geometry of the model is constructed from MR data, and its mechanical properties are modeled using a nonlinear material model. The breast is compressed, and the FEM is used to predict the position of the tumor during the procedure of compression. Also, deformable models of breasts were built by this team, virtually compressed, and used to predict tumor positions in the real compressed breasts.

This team encounters some problems with the MR imaging-guided localization technique which they developed that would not happen in a breast ultrasound-based system, such as de dependence on the injection of a contrast-enhancing agent, which makes the lesion appear clearly only in the two minutes that follow its injection. After that, the signal loses intensity and the boundaries of the lesion change.

However, there are some problems in common between the MR and breast ultrasound techniques for needle guidance, which concern the needle itself: it is not very sharp, and its insertion may not be as smooth as wanted. When the tip of the needle reaches the interface between two types of tissue, continuing its insertion will cause the tissue to be pushed, not pierced, causing unwanted deformations. Compressing the breast as much as possible would minimize internal deformations caused by the needle, but would make the blood be squeezed out, alter the shape of the lesion in the imaging technique and would be highly uncomfortable for the patient.

The limitations of needle placement and breast deformation make needle procedures very sensitive to the initial needle placement and breast compression. It is not easy to tell whether a specimen removed during a biopsy clearly corresponds to the lesion of interest, given these added difficulties that impair the location of the tumor boundaries.

As the team creates a breast model and uses it in a virtual reality system for needle-guidance in biopsy, they also advert that creating very complex models, which can be thought as a necessity for the process, can prevent them from being useful clinically due to excessive complexity and computational time.

The three-dimensional mesh model is created by the team in a custom-written program in C, BreastView, that takes as input a set of breast contours and its segmentation results, and generates the FEM, allowing volume elements to be scaled to any size. So as to model the skin, the team uses three-node triangular isoparametric elements, and to model the breast inner tissues, the team uses solid eight-node hexahedral trilinear isoparametric elements. All elements are assigned nonlinear material properties and each element corresponds only to one type of tissue, the one that is more abundant in the element's region. For higher accuracy in the lesion region and enhanced computational speed, the mesh density is increased around the point of interest and decreased away from it.

To model large deformations such as the ones caused by compression plates in MR imaging methodologies, the team divides the displacements in small steps, and, for every small displacement step, uses the small strain theory. Strain is calculated using the Cauchy infinitesimal strain tensor formula.

As they are interested only in slow displacements, the great majority of forces applied to the breast tissues can be attributed to an elastic response. This is done even though most biologic tissues display both a viscous (velocity dependent) and an elastic response. Also, the tissues are considered isotropic, homogeneous, incompressible and with nonlinear elastic properties. This being assumed, the team finds a way to define the mechanical behavior of the breast tissue with a single elastic modulus, which is a function of strain on a specific tissue type and the applied stress on that tissue type. This is a nonlinear relationship, calculated for every tissue type from uniaxial stress-strain experiments performed with tissue samples. Then, the experimental curves are fit to a material model, which is characterized by a small number of parameters. To create stress-strain curves (nonlinear), the team needs mechanical properties of breast tissue, which they take from previous literature.

The elastic modulus $E_n$ for tissue type $n$ is given by:

$$E_n = \frac{\partial \sigma_n}{\partial \epsilon_n} = b_n \cdot e^{m_n \epsilon_n},$$

Where $\sigma_n$ is the nominal stress, $\epsilon_n$ the nominal strain, for tissue type $n$, $b_n$ and $m_n$ are the fit parameters determined experimentally for each tissue type.

For glandular tissue, $b_{gland} = 15{,}100\ N/m^2$, $m_{gland} = 10{,}0$, and for adipose tissue, $b_{fat} = 4{,}460\ N/m^2$, $m_{fat} = 7{,}4$. The team used a value of 0.49999 for the Poisson ratio.

As for skin, the experimental stress-strain curve is transformed into a piecewise linear stress-strain curve, used to describe the mechanical properties of skin in the breast model. The skin elasticity modulus, $E_{skin}$ is function of the strain, $\epsilon_{skin}$, and is given by:

$$E_{skin} = a_i, (i = 1\ to\ 3)$$

The values for $a_i$, which make the function piece-wise, are, 3.43 x $10^6$ (for $0 \leq \epsilon_{skin} \leq 0.54$), 2.89 x $10^7$ (for $0.54 < \epsilon_{skin} \leq 0.68$), and 1.57 x $10^8$ (for $0.68 < \epsilon_{skin} < 1$ ). The third range of values for $E_{skin}$ represents the elasticity of skin tissue at very high strains ($\epsilon_{skin} > 0.68$); skin tissue becomes very stiff due to the presence of the collagen fibers, whose effect is much more prevalent than that of elastin fibers at higher strains. As a practical matter, such high strains never occur with breast tissue during an interventional procedure.

The material studies of this team go beyond previous assumptions and property measurements that were not done in conditions that completely simulate those in vivo. Studies normally ignore the supporting structure of fibers in the breast, the measurements are almost made at room temperature, that can be 10º to 15º lower than body temperature, markedly changing the mechanical properties of breast tissue, which is almost liquid at body temperature but not at room temperature. They hypothesize that the supporting structure of fibers, such as Cooper ligaments, compartmentalizes fatty tissue, preventing it from being squeezed out of its location, and that the compression of fatty tissue increases the local pressure and the apparent stiffness value of fat. However, instead of modeling the structure and geometry of the Cooper ligament, the team models their functionality and overall effect. For that, they model the elastic modulus of fat with a quadratic equation with unknown parameters that are to be determined from the given boundary conditions. These conditions state that, at zero strain, the elasticity modulus of fatty tissue is the same as the experimentally derived value used in the previous equations; for a strain lesser or equal to the limit strain, the elasticity modulus of adipose tissue is greater that its value for $b_{fat}$ at zero strain, but smaller than the elasticity modulus of glandular tissue, and the slope of the adipose tissue elasticity modulus function is positive, meaning that it is nondecreasing. When the strain is at its limit, the conditions state that the elasticity modulus of fatty tissue is equal to that of the glandular tissue and the slopes of the functions of elastic modulus for glandular and fatty tissue are the same. When the strain on fatty tissue goes above the limit, the stiffness of fatty issue is always the same as the stiffness of glandular tissue.

On **figure 17,** one can see the structure and location of Cooper ligaments and the fat material properties curve, affected by the cited fibrous structures through the modeled equation with boundary conditions.

For model dynamics, the team uses the finite element method, as stated, through which all quantities necessary for the Lagrange equations of motion are derived from the same quantities computed independently within each finite element (they do not assemble the matrix for the model stiffness, as they work individually with elemental stiffness matrixes and assemble the forces around the nodes).

The **figure 18** contains the uncompressed MR sections for three patients, containing lesions and the corresponding uncompressed model sections, containing lesion elements.

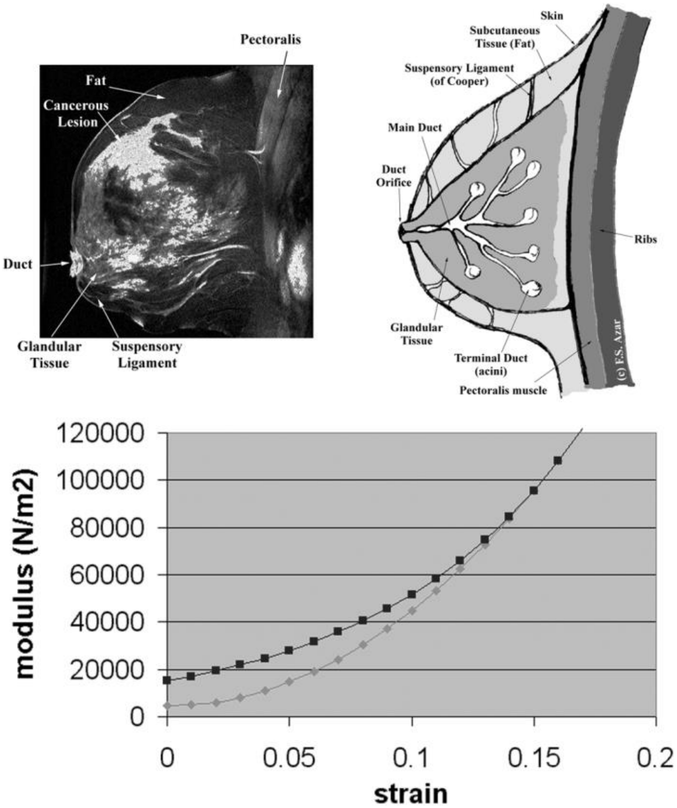


*Figure 17 – structure and location of Cooper ligaments, on top, and fat material properties curve, on bottom. The diamond mark represents $E_{fat}$ and the square mark represents $E_{gland}$*

The chapter 10 of [14] sums up many techniques of 3D patient-specific modeling of breast anatomy and simulation of breast biomechanics, such as the ones presented previously in this overview. They state that breast models have been created predominantly from MR images, but also from computed tomography images. They also describe segmentation approaches of the boundaries of the breast from the same images, which include intensity thresholding with morphological operations and edge-based constraints. The FE models play a role with considerable relevance in the field, and the meshing algorithms employed to construct them go from Delaunay triangulation to marching cube algorithms. Tetrahedral and hexahedral elements are the most widely used types in FE meshes and are usually interpolated using standard Lagrange-based interpolation schemes, such as the linear or quadratic Lagrange shape functions.

The presented works in the cited review may pay attention to the need of segmentation of fat, fibroglandular tissue, pectoral muscle and tumor tissues. The followed approaches vary from manual segmentation to thresholding or fuzzy C-means.

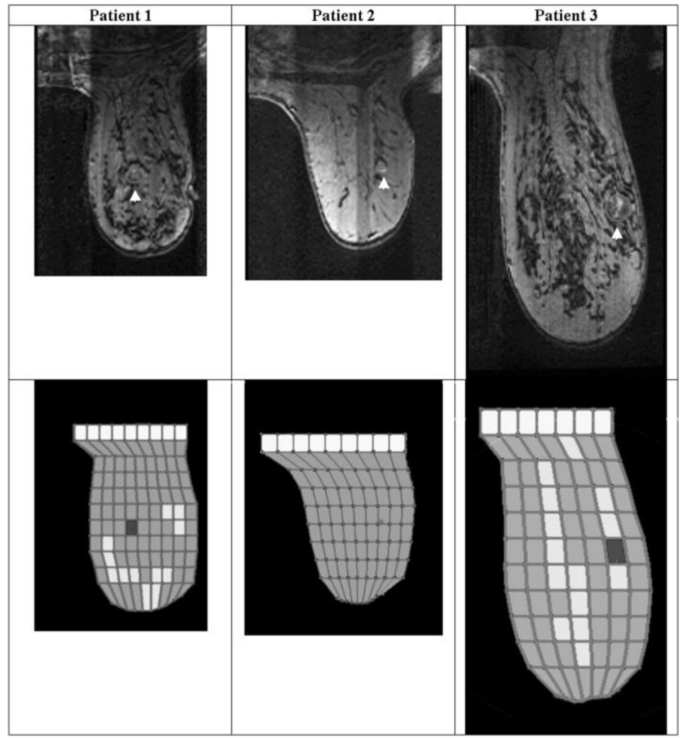


*Figure 18 – uncompressed MR sections for three patients, containing lesions (arrowheads), on top, and corresponding uncompressed model sections, containing lesion elements (bottom)*

They also state the difficulties on modeling Cooper's ligaments, seen before, saying that, even though they have not been explicitly modeled yet, their mechanical influence has been indirectly investigated. Remaining structures and vessels (for blood or lymph) are usually not modeled discretely, since their contribution to the overall mechanical response is assumed to be minor compared to adipose tissue, fibroglandular tissue, skin, and even Cooper ligaments.

As for simulating breast biomechanics, [14] sums up what has already been concluded: the breast tissues are typically constrained to be incompressible due to the large water content; small and large deformations are treated differently, either considering linear or pseudo-nonlinear elasticity. For larger deformations, as mesh distortion can be problematic, researches have employed remeshing algorithms.

Pseudo-linear elasticity, which assumes the linear elastic modulus is a function of strain, is recurrently used to model breast compression for biopsy procedures, and to simulate deformation due to gravity in the standing position.

*3) Tracking tumors for surgical assistance and biopsy*

A brief review on the topic of tumor tracking during surgical procedures is presented on [14]. In what concerns surgical procedures, these are performed usually in the supine position. As this position may differ from the ones adopted during diagnostic imaging, such as the prone position during MRI, biomechanical models are used to track tumors from their location in the imaging methodology procedure to their location during the surgical procedure.

To register prone and supine MR images, fluid registration and B-Spline free-form deformation registration have been done, and the aid of stereoscopic camera systems is being considered to determine the locations of tumors in the breast during surgery, recurring to biomechanical models.

MR images and also breast ultrasound images may be acquired in supine position, what does not stop the breast from positioning itself differently during imaging procedures and during surgery. To account for this possible deformation, a stereoscopic scan of the breast surface can be obtained while the patient is on the operating table, and used to provide boundary conditions for deforming the supine model to the surgical configuration.

On biopsies, the problematic differs, since the proposed methodology is to guide the needle inside the breast using an ultrasound probe. Even though the deformations are being observed in real-time while the needle is being inserted, the simulation of this procedure is relevant, resulting in a need for needle insertion modeling and simulation.

The work done in [21] presents an answer to this problem: they aim to estimate the force distribution that occurs along a needle shaft during its insertion. Then, this distribution may be used for graphical and haptic real-time simulations of needle insertion. This study may also contribute to needle placement optimization, trajectory planning and automatic control of the biopsy needle.

Needle forces use to be determined only for the proximal end of the needle, but, in fact, penetration forces are distributed along the entire length of the needle axis, resulting from physical phenomena such as cutting, elastic deformation and friction (static, kinetic and viscous). Not only a tissue deforms when a needle penetrates it, but also the forces in the needle vary, being applied axially and laterally. The deformation of the tissue affects the path of the needle.

The team creates a soft tissue phantom with properties approximated to the ones of breast tissue (Young's modulus below 10 kPa) but varies the properties to cover many of the body's soft elastic tissues (Young's modulus up to 100 kPa). The phantom is molded from polyvinyl chloride (PVC) and a liquid plasticizer (phthalate ester – by varying its amount, one can produce phantoms with the cited different elasticities).

To know the response of the phantom to needle penetration, known forces are applied to the tissue phantom's boundary while measuring the resulting node/marker displacements. Also, from the resulting deformations and applied force, the distribution of force applied along the needle shaft can be computed.

The needle force distribution that is estimated from experimental measurements, and used for simulation, indicates that axial forces between the needle and the tissue phantom are relatively uniform along the needle shaft. A force peak, located immediately behind the needle tip, rises approximately 100% above the shaft force, and may be attributable to tissue cutting.

The team creates a FE model for simulated needle insertions and compares the node positions to measures made in the phantom. The estimated force distributions are used to estimate the node positions in the FE model. This can be seen in **figure 19.**

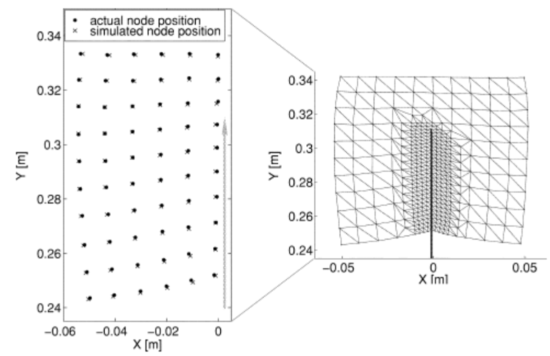


*Figure 19 – comparison between measured and simulated needle insertions (using the estimated force distribution). Left: sample of the measured and simulated node positions from one half of the phantom (the deformation is symmetric)*

## III. Methods

### A. Preliminary studies

The methods to investigate the research questions aim to produce the necessary tools to quantify deformations in the breast phantoms and to do quantitative and qualitative elastography studies using ultrasound imaging and an absolute referential grid.

Not also the algorithms for automatic measurements had to be developed and improved, but also the PVC phantoms with an embedded referential grid had to be produced through an optimized method for this specific study.

The final algorithm approach for deformation visualization is to take the PVC phantoms with embedded fishing lines as a grid, and apply forces while recording deformations in a 2D, with an ultrasound probe. The grid displacements give information about the local deformations, when external forces are being applied, but also when a needle is being inserted. The same grid displacements, related to the correspondent external forces applied, give information about local and global stiffness of the phantom.

#### 1) Phantom fabrication

The phantoms made in the scope of this project have different compositions, being based on polyvinylchloride (PVC), plasticizer, hardener or softener, fishing lines, and, in some cases, silica gel.

The stiffness of the material is controlled by the concentration of plasticizer on PVC, being that inclusions that are made to simulate lesions are composed of stiffer PVC than the bulk of the phantom. One must take in account that a stiffer material results in a region in the phantom with more acoustic impedance.

The referential inside the phantoms is made, in the final phase of the project, in which most of the results were acquired, of parallel fishing lines, placed regularly through the phantom. In an initial phase of the project, few lines were included in the phantom, since the focus was the design of a referential solution that would be perfectly visible through ultrasound imaging and not yet the displacement calculation, when the phantom is subjected to certain forces. Initially, the author tried to make referential lines out of the same material as the rest of the phantom, adding silica gel (1% m/v of silica gel on strong PVC) to increase, locally, the echogenicity of the material, without the problematic of the influence of fishing lines in the stiffness of the phantom.

The initial line positioning methods that are shown in figure 20 evolved to the creation of a 3D printed box with precisely placed holes on two parallel walls, through which a defined grid of fishing line is inserted.

To assure that the background is anechoic and that the only echogenic regions are the gridlines of the referential, the fishing lines, one must assure that nothing compromises the anechoic property of the background. This property can be hindered by the introduction of air bubbles in the bulk of the phantom, since these air inclusions are more echogenic than the background, so it is possible that the gridline detection algorithm perceives air bubbles as points that correspond to the referential lines' circular sections – the gridpoints. This problem is even more visible if the bubbles have the same size and shape as the referred gridpoints, which is likely, since they are circular and can have a radius of around 1 mm.

The PVC solution, depending on its proportion in relation to plasticizer, needs to be heated to a certain temperature (which increases with the concentration of plasticizer) so that its polymerization is possible. It is in a particle solution, and, when heat is applied, the particles dissolve and cross-link. Then, lowering the temperature of the material makes it become solid.

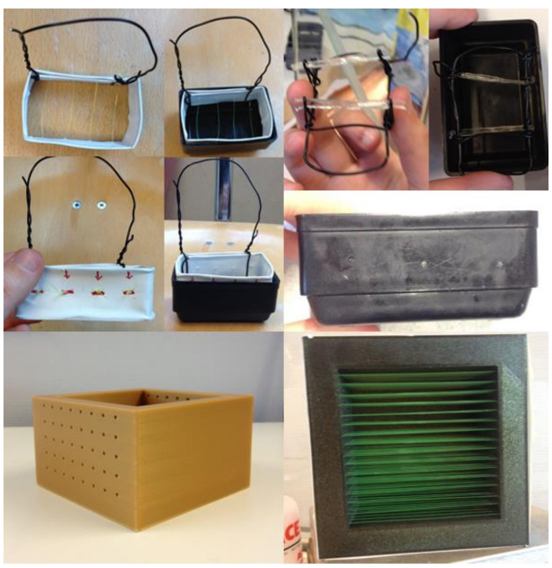

*Figure 20 – methods of referential line placement. The first images on the left represent the first method, that would only place four lines, using wire, tape and a small plastic box. On the right, a similar method was used to place PVC and silica gel lines (only two). The box under this image on the left has holes on two of the parallel walls, working in the same way as the first example on the right. The bottom molds are the 3D printed boxes, with holes for the line insertion. The one on the left has more space between the holes than the one on the right, and the latter is shown with the lines already placed.*

MURAB's approach to phantom development is to build 3D printed casts and fill them with PVC solutions of different thicknesses. PVC is mixed with plasticizer to create thicker structures, such as the skin. The skin portion of the breast is built first, pouring stiffer PVC in the main mold and pressing a counter mold against it to create a skin layer. When this layer is solid, softer PVC can be poured inside it, to simulate the softer adipose and fibroglandular tissues. For the breast base, a stiffer PVC solution may be used.

For this specific project case, lesions were simulated, instead of skin or normal tissue types: the lesions are inclusions of stiffer PVC placed inside the bulk of the phantom.

The brands of PVC, plasticizer, softener and hardener used for the fabrication of phantoms in this project are *LUPA (Plastisol)* and *Bricoleurre (Plastileurre).*

The PVC is heated to around 200 ºC (temperature depending on the concentration of plasticizer) in a regular pan, through a heating plate with an incorporated thermometer that allows for temperature control. Then, for air bubble removal, either the pan is placed in the pre-heated vacuum oven at the same temperature as it was being previously heated, or the PVC is poured in the mold and placed in the vacuum oven at room temperature, so that there is no danger of the mold melting. The placement of the PVC in the vacuum oven should release all the air bubbles from it.

This project's molds have a regular parallelepipedal shape, contrarily to MURAB's phantoms, which try to simulate the breast shape.

The molds for the phantoms were created with fixed base area but variable height so that the amount of lines placed in the phantom can be variable. The phantom mold, along with the gridlines placed inside it, are previously sprayed with a non-stick coating, to ease the process of removing the phantom from the mold when it is ready.

Because the gridline referential placement inside the phantom makes the process of inclusion of different thickness portions of PVC, to simulate lesions (**figure 21**), more difficult, the author's strategy evolved from previously placing already solid "lesions", making the fishing line go through them, already inside the mold, and pouring molten PVC afterwards, to create the rest of the phantom, to creating a provisional inclusion that is designed to have slots that allow for it to be placed in the phantom mold with the lines already inserted in it. This provisional inclusion is removed when the PVC external to it is solid enough to leave a counter mold for the pouring of stiffer PVC, that will create the lesion.

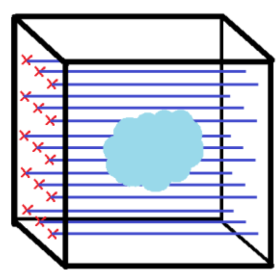

*Figure 21 – schematics of a phantom with an included lesion, showing that the lines must go through it as they go through the remaining parts of the PVC structure*

*2) Lesion and needle tracking in ultrasound videos*

Using a phantom with anechoic inclusions and a hyperechoic background, whose echogenicity is caused by the presence of silica gel in the constitution of the phantom, several attempts, using different techniques, were made to keep track on the lesion while an ultrasound exam is being performed. The videos in which the anechoic lesion is segmented and identified in every frame, keeping its track, are recorded moving the probe in random directions, above the lesion. Given the two-dimensional character of the ultrasound exam output, creating a profile section image in several locations of the probe, the lesion changes shape and its surroundings change in every video frame.

As recommended by [22] ,an algorithm for breast ultrasound image analysis should involve the following steps: pre-processing, to increase the contrast between the lesion and the background, which can include a low-pass filter, to reduce speckle artifacts; segmentation, which separates the lesion and the background (other tissues); morphological and texture feature acquisition, creating discriminative properties of the classes (lesion/non-lesion, lesion/fatty-tissue/glandular tissue, etc.); and finally the classification, preceding or not a post-processing algorithm. This pipeline describes the generality of CAD (computer aided diagnosis) systems.

As for the tracking of an anechoic lesion in an echogenic background, the author used an entropy filter of each grayscale frame of an ultrasound exam video. An entropy filter is a texture filter which gives a statistical measure of randomness. This randomness provides information about the local variability of the intensity values of pixels in an image. In areas with a smooth texture, as the anechoic lesion bulk, the entropy is low because the range of values in the neighborhood of a pixel is small. In areas of rough texture, caused by the silica gel in the PVC constitution, in the background of the lesion, the entropy is higher. This way, the entropy image can be segmented through a threshold that can separate the lesion and the background, segmenting the region of interest (ROI): the pixels of the image that have smaller values of entropy. After the entropy filter, the author computes the image negative and does histogram equalization, which adjusts the image contrast through its intensity histogram. Since the image was filtered with an entropy filter, the histogram used has entropy levels. Histogram equalization spreads the most frequent values, stretching the intensity range of an image. After histogram equalization, circular hybrid median filter is performed on the image. This is done for despeckling the ultrasound image. The speckle phenomenon is translated into multiplicative noise that degrades image quality. Because speckle noise is granular, a median filter can be indicated to remove it. A hybrid median filter is an improved version of a regular median filter: it can remove impulse/salt and pepper noise while preserving corners, helping to keep the shape of the lesion as intact as possible [22].

After this pre-processing in the image, a regular Otsu thresholding is applied, followed by the deletion of regions that are too small or too big to be part of the lesion.

The centroid of the found lesion (the set of ones in the result of Otsu thresholding) is calculated for each frame, so that an automatic indicator of the presence of a tracked lesion in the frame is generated. This way, if no centroid is found, which means that no lesion is tracked in a certain frame, a wider detection threshold is applied, which means that both smaller and bigger than the previously considered blobs are considered now. This can prevent valid lesions from being discarded because their size is altered during pre-processing. Also, if this doesn’t work, pre-processing phases are not considered, and morphological opening is introduced, to create distinguishable blobs (**figure 22**).

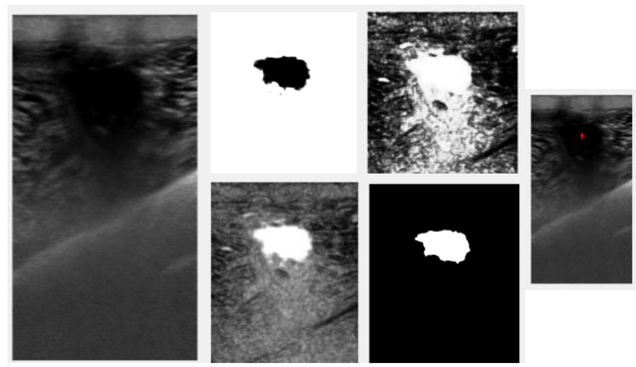

*Figure 22 – the first image shows a detail with a lesion in an ultrasound video frame. From the left to right, the first image shows the result of the entropy filter in the image. Under it, one can see its complementary image. On the upper-left is the result of histogram equalization operation. Under it is the result of the application of hybrid circular median filter to the previous image. The last image represents the calculated centroid position for this image.*

In order to track a needle in an ultrasound video, one may assume that the metallic material of the needle makes it more echogenic than the background and that the shadowing effect that it creates has increased pixel intensity in comparison to the neighborhood pixels. A generalized increase in the intensities in the image histogram may mean that a needle insertion is occurring.

Because both needle tracking and lesion tracking algorithm approaches may interfere in the referential grid tracking of the upcoming algorithms, they are not considered in the further sections and final results.

*B. Deformation tracking and elastography*

*1) Gridpoints tracking algorithm*

To calculate the deformations caused by the application of a certain force in the surface of a phantom, the circular section of every gridline – its correspondent gridpoint for a 2D plane – must be tracked, and the distances between every gridpoint and its neighbors must be calculated. The distance between a gridpoint and its neighbor, in the horizontal plane, is supposed to decrease if a compression in the horizontal plane is performed. Moreover, if the compressions are done inside the elastic limits of the phantom material, the relative decrease of distance between points should be related to the applied compression through the elastic modulus of the material in the specific location where the two neighbor gridpoints are placed.

Several attempts were made to create an algorithm that could correctly segment and track the gridpoints in each video frame. The author started by trying to identify which image features could differentiate the gridpoints from the background and from the air bubbles present in the phantom. Also, the artifacts caused by the ultrasound image technique needed to be considered and their effects removed or ignored by the segmentation algorithm.

The initial pipeline for gridpoint tracking and measuring the distance between every gridpoint and its direct neighbors started with applying a median filter to the image, to remove noise related to possible air bubbles. Each output pixel of this filter contains the median value in a customizable neighborhood around the corresponding pixel in the input image. As stated before, a median filter preserves edges while removing noise, maintaining the shape of the gridpoint blobs. After denoising, morphological operations of opening by reconstruction, followed by closing by reconstruction, are performed. These aim to remove elements smaller than a certain structuring element and keep the shape of the blobs that are not to be deleted. These two operations work sequentially in the image in grayscale and remove high intensity noise, expanding the remaining high intensity regions afterwards (**figure 23**). This initial pipeline proceeds by calculating the regional maxima of the resultant image of the previously mentioned pre-processing. This step would later be replaced by an Otsu segmentation. After binarizing the image through this process, the connected components present in it would be analyzed in terms of eccentricity, solidity and area. A threshold for these properties would be applied, and only the components that would fit in the characteristics of a gridpoint-like-blob would have their centroid calculated. Characteristics of a gridpoint-like-blob would include an area of more than 200 pixel, since smaller blobs could be considered air bubbles, an eccentricity lower than 0.95 (this is the eccentricity of the ellipse that contains the same second-moments/area moment of inertia as the blob region, calculated as the distant between the foci of the ellipse and its major axis length, being 0 for a circle and 1 for an ellipse that is actually a line segment), and solidity higher than 0.75, which means that the percentage of the pixels in the convex hull that are also in the region must be at least 75%. The Euclidean distance between centroids would be, then, computed.

Cascade classifiers in combination with LBP (Local Binary Pattern) features were investigated for gridpoint tracking, but were found to be complex and not very useful.

Detection and tracking problems would arise when symmetric reflections on the bottom of the phantom (ultrasound image artifacts) would be accounted as gridline points, and bigger air bubbles (the ones that would not be removed by opening and closing by reconstruction or by feature thresholding) that had intensities in the same range as the gridpoints would also be mistakenly considered.

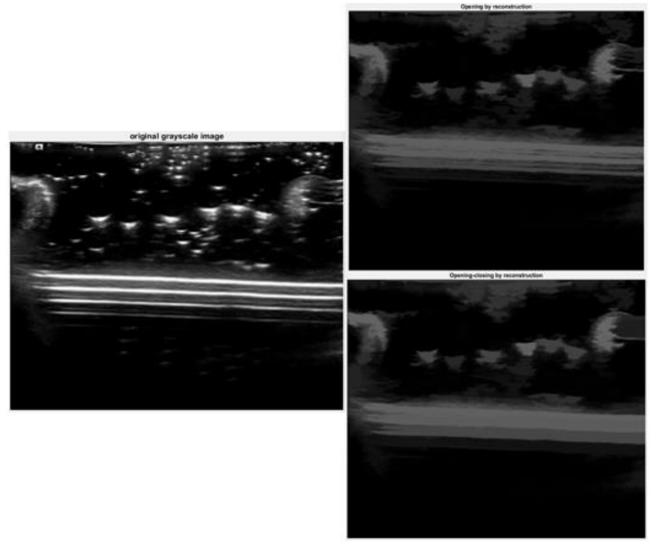


*Figure 23 – On the left, a grayscale image of a phantom created in an initial phase of the project. It shows a 2D section of a phantom and six gridlines crossing it. On the upper-right, the result of opening by reconstruction, which deletes the noise caused by air bubbles. The last image is the result of the latter operation followed by closing by reconstruction, which widens the higher intensity areas.*

The symmetric reflections problem was solved by segmenting the image automatically by the reflection plane. This required detection of the reflection plane, which is defined by being a large high intensity area in the middle part of the image. For this to happen, the eccentricity, area and equivalent diameter (diameter of a circle with the same area as the region) of each connected component present in the image are analyzed, and these measures are thresholded, so as to collect only the blob-like objects and not the stretched lines that mark the reflection plane. The reflection plane is defined by a greater eccentricity, area and equivalent diameter than the remaining connected components. The image is cropped in a rectangle that contains the portion above these stretched objects.

The approach with better results for the segmentation and tracking of gridpoints was reached using the following pipeline, implemented in a guided user interface: in the first frame of the ultrasound video, the user is asked to crop a region of interest, after choosing the format of the grid (either 5 lines and 6 columns, 5 lines and 7 columns or 5 lines and 10 columns). This region of interest should correspond to a portion of the first frame that contains as many points, in the same format as the chosen grid. If one chooses a 5 by 6 grid, one should select a region with 5 lines and 6 columns of gridpoints (**figure 24**). Then, if this region of interest happens to have the ultrasound system watermark in the upper-left corner, the user can choose to remove it, also selecting a region around it in the first frame, which will be left as zeroes until the last frame of the video.

The remaining frames are read, one by one, and cropped in the same regions as the first one. Then, they are converted to grayscale and an initial morphological closing operation is applied to make the gridpoints more solid and the higher intensity regions wider.

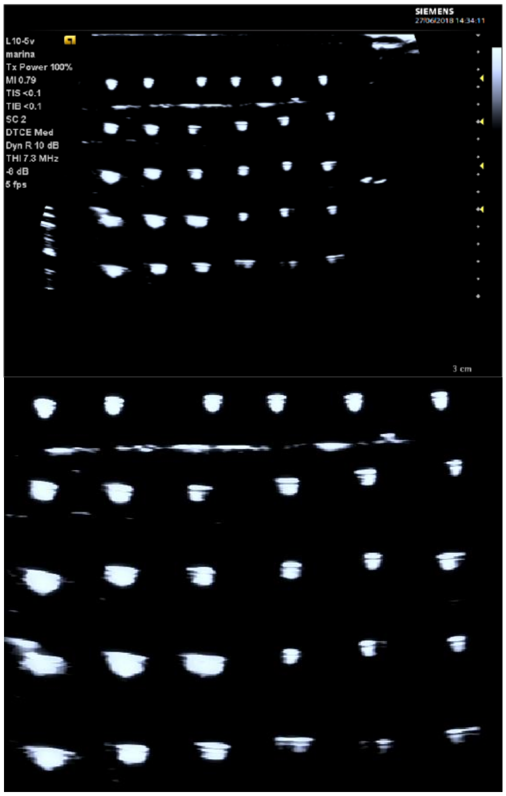


*Figure 24 – the upper image is the first frame of an ultrasound video. Under it, the result of selecting the region of interest when the user wants to analyze a 5x6 grid.*

Then, the process continues with an algorithm that creates horizontal and vertical intensity profiles in the image and computes a correlation grid.

To create the intensity profiles, it calculates the mean intensity in the y and x directions. Then, it searches for an equation, $f = \sin(ax + p)$, that has an optimal correlation with the horizontal and vertical profile intensities. In the equation, $a$ stands for the frequency, in Hz, $x$ for the pixels in the vertical or horizontal direction and $p$ for the phase shift. The points in the image whose intensity is higher (in average in x or y direction) will correspond to peaks in the intensity profiles. These peaks should correspond to the maxima in the waveform that is optimally correlated to the intensity profiles of the image. To find this optimally correlated waveforms, the algorithm tries 163 increasing frequencies, from a minimum of considering only two full waves (two intensity maxima) to ten full oscillations. Correlation coefficients are calculated, as measures of similarity between the calculated waveforms and the intensity profiles of the image.

The waveform that allows for the best correlation is shifted in phase to align with the intensity profile in the calculation direction (**figure 25**). The waveforms in the x and y directions are combined and the peaks of this combination are spatially plotted. The waveform peaks in the x direction contribute with the x coordinates for the plotted points and the peaks in the y direction with the y coordinates. The peaks of this resultant waveform are taken as references for searching for gridpoints in the image. Later, a circular region of interest is created around each one, and the tracking algorithm will only look for points inside this area.

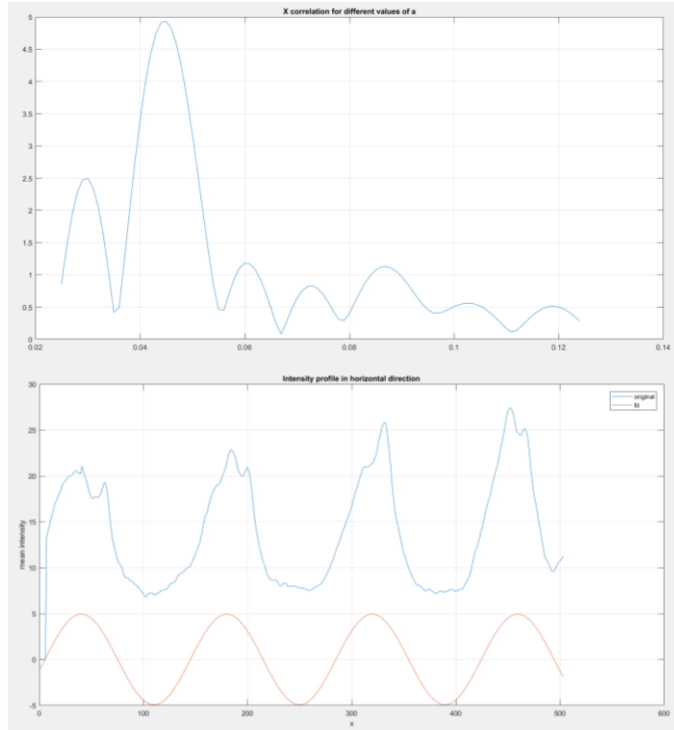


*Figure 25 – the upper plot shows correlation values for different values of frequency in the horizontal direction for an example image. In this plot, one can see that the bigger peak corresponds to the frequency of the waveform that is better correlated with the intensity profile of the image in the x direction. Under this plot, there's another one with two curves. The blue curve represents the original intensity profile of the example image in the horizontal direction, and the red one is the waveform created with the frequency found by the greatest correlation (peak in the upper plot) and a phase shift correspondent to the phase shift in the horizontal intensity profile.*

Around the plotted peaks of the correlation grid previously calculated, a search radius is dynamically set, to create circular regions where the gridpoints are looked for. These regions have a radius correspondent to the height of the image divided by 2.3 times the number of lines of gridpoints present in the ultrasound film. The division of 2.3 times the number of lines was iteratively selected, knowing the usual size of the gridpoints, in order to create circles around the peak points that wouldn't overlap or be too small (**figure 26**).

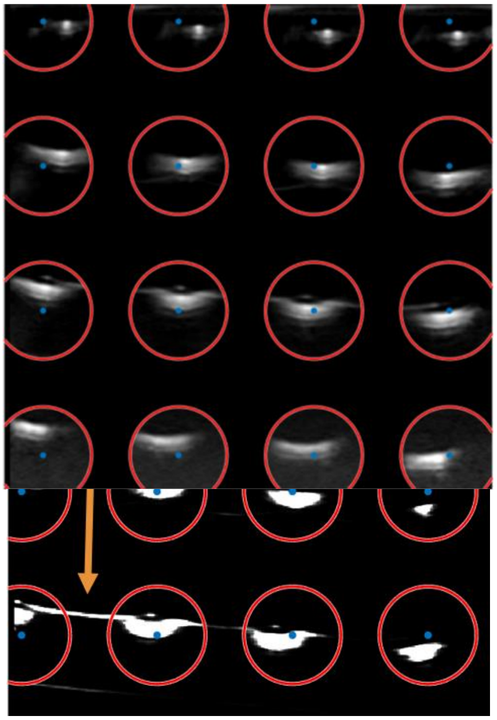

Figure 26 – in blue, the plotted peaks of the correlation grid. Around them, limited by a red circumference, the search area, in which the algorithm will proceed to look for blobs, gridpoint candidates. The bottom image shows a detail on the already processed upper image: artifacts of the ultrasound imaging may create elongations of the gridpoints that shouldn't be considered in the gridpoint tracking, like the one pointed by an orange arrow. Defining a search area prevents these artifacts from being considered in the final result.

Inside this circular search regions, the processing is now individually done. This personalization of methods is implemented because ultrasound imaging has the particularity of differing in terms of quality and artifacts with the depth of the ultrasound wave profusion. Since the ultrasound wave gets diffracted, it loses energy as it goes deeper in the phantom. Lowering the frequency of the ultrasound wave helps creating detail in greater depth, in relation to higher frequency waves, but compromises quality. In this case, because the aim is to reach 3 to 4 cm deep in the phantom, to track as many lines as possible, the lowest frequency of the ultrasound system is chosen, favoring depth of analysis over detail. The frequency used for the imaging process is around 7 MHz.

The content of each and every circle is individually filtered, if its intensity is not globally zero, with a mapping function that tries to lower even more the low intensity levels and keep some of the high intensities, and after this, with a 2D Gaussian smoothing kernel with a standard deviation of 1. The mapping function used has a concave shape defined by a parameter *gamma* of the MATLAB function *imadjust*, of 2.5, which weights the mapping toward lower (darker) output values. A representation of a mapping function with this property is in **figure 27**. If the output of this mapping results in an image with no intensity levels above the threshold of 45, then this filtering is not applied.

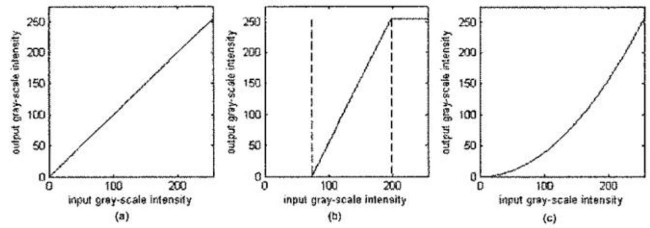


Figure 27 – mapping functions used in grayscale images. The first one corresponds to the identity transformation. The input image (x) has the same intensity values as the output image (y). The second function takes only the intensities inside a certain range of the input image, stretching this range to a 0-255 interval. The third function weights the mapping toward dark output values.

After filtering, Otsu thresholding is applied differentially to each search area. Because of the separation of the image in individual areas, the intensity threshold levels are different for each circle. This is of great utility because the image quality worsens with depth, and there is a need for a different threshold for upper and lower areas in the same image, since the loss of image quality translates into the appearing of higher intensity noise, shifting intensity histogram global values to higher numbers with depth.

The number of connected components in each circle is calculated, so that one can make sure that only one gridpoint can be tracked in each search region. If there is more than one connected component in a certain blob, then the gridpoint candidates that are not the real gridpoint must be deleted. This is initially attempted by merging small components into one through a morphological closing operation with an increasing structuring element. This structuring element is a disk with a radius from 10 to 40 pixels. When the radius of this disk reaches 40 and there is still more than one connected component inside a search area, another method is followed: the distance from the search circle center to the centroid of each connected component is calculated as a parameter of exclusion – only the blob closer to the center of the search area is kept.

To identify each segmented gridpoint and follow its specific trajectory in further processing, each gridpoint is given a color through the creation of a chess-board-like grid with squares that have different and unique colors and that are centered in the search region centers. This means that there are as many squares as search regions and that they move together with the different placement of the search regions, for each frame, allowing for the gridpoints to be correctly colored in each frame. There is only one color assigned to each gridpoint and there are no two gridpoints with the same color (**figure 28**).

The position of the gridpoints' centroids and the color for each gridpoint are saved in the same matrix, that is used in the remaining steps of the algorithm.

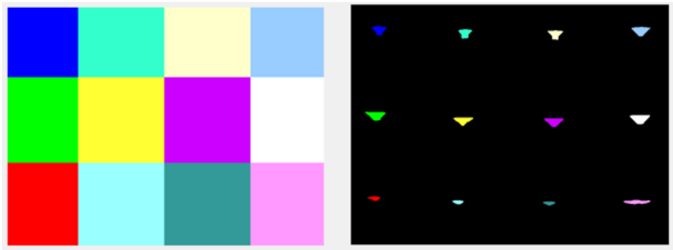

*Figure 28 – dynamically colored grid that gives a unique and identifying color to each of the gridpoints in an image*

Using the said gridpoints' centroids and color matrix, one can plot the path of every point individually in a certain ultrasound video, as can be seen on **figure 29**. Through the analysis of the centroid path in a video that follows the extension of the gridlines, with a probe trajectory perpendicular to their placement, going from the lines' start to the lines' end, the **figure 29** is obtained. Because the lines are supposed to be parallel, the centroid shouldn't have had moved from its initial point (final movement showed by a black arrow in each trajectory) as much as it did in this specific video. The problem associated with this kind of analysis is that either the probe or the phantom, or both, are mobile, and their movement should be as controlled as can be. Also, if the lines are not completely parallel, the same error will be introduced. A video of an ultrasound scan that is supposed to show the relative movement of gridpoints, when the phantom is subjected to external pressure or needle insertion, will not only show the movement of the gridpoint but the erroneous movement of the probe (that is supposed to be fixed, and its movement may be taken mistakenly as the gridpoints movement) or of the phantom (translational movement not caused by the compression), or even by the lack of parallelism of the lines. The latter effect may cause that, if the probe gets slightly out of the 2D plane that is to be analyzed, the gridpoints won't be situated correctly anymore because the lines' placement doesn't allow for the same location of the successive line sections, creating unwanted movement.

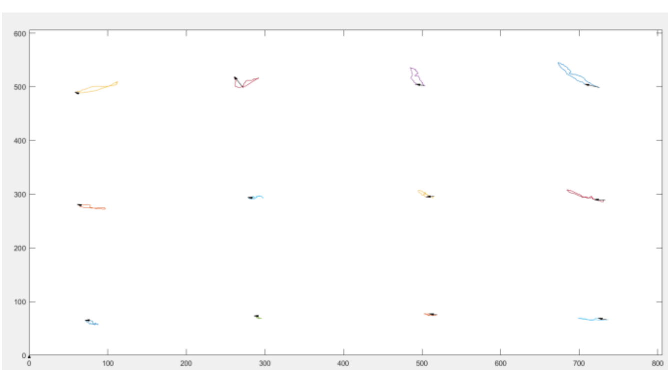

*Figure 29 – trajectory of each gridpoint in a video following the direction of the gridlines. It shows the effect of when lines are not completely parallel, together with a possible deviation of the probe from a linear route, and also a possible translational movement of the phantom itself. In this case, the effects are very visible because the phantom with which the video was made had problems in terms of line placement – the lines deviated from the parallel position in some places, increasing the error. In the further phantoms, this effect is less present.*

*2) Local deformation calculation algorithm*

Taking the matrix with the position and the identifying color of each gridpoint, for each frame in a video, the local deformations, it is, distances between neighboring points, can be calculated.

The distances considered are the ones between a certain point and its four direct neighbors, not considering diagonal distances. Only the x direction distance between two points is considered if the points are related horizontally, and the y direction distance, if the points are placed vertically in relation to each other.

The calculated distances for the first frame, in which the phantom should be in a stable equilibrium position, are taken as references, so that the following distances in the following frames can be compared with the equilibrium state.

Lines between the gridpoints are drawn in an image, filling it with horizontal and vertical segments that correspond to the distances between the gridpoints and its neighbors, in the horizontal and vertical directions. These lines are colored afterwards, according to the fraction between their length and the length of the reference lines, in the first frame. This way, one can see if the phantom is either being compressed from its equilibrium state or if tensile stress is being applied. In a case in which the ultrasound probe is placed on the side of the phantom, fixed in a position perpendicular to the gridlines, if the vertical distances decrease and the horizontal distances increase, there is either a compression happening in the vertical direction or a tensile stress in the horizontal direction, perpendicular to the probe placement (**figure 30**).

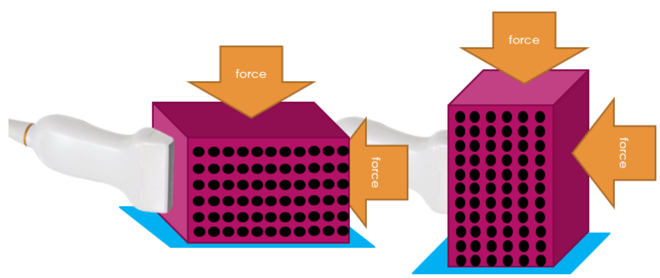


*Figure 30 – Probe placement and compression directions whose images can be analyzed via the proposed method. The deformations are done with a fixed probe, and for elastography purposes (later), only the forces perpendicular to the surface in which the phantom stands (in blue) are accounted, because of the influence of the probe in the normal reaction, if the forces are applied parallelly to the surface.*

The lines are colored differently if they are being shortened or stretched, being that their color varies with the amount of shortening or stretching, relatively to the initial equilibrium position. The colormap for better perceiving the lines stretching and shortening is on **figure 31.** It is designed to have high contrast around the middle of the full scale, so that deviations from the equilibrium can be easily seen. The equilibrium point, which means no compression or extension relatively to the reference, is colored in green, in the middle of the scale range. The colormap was created by adjusting a regular *jet* colormap with 64 color bins.

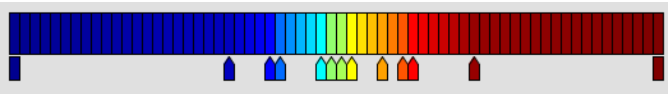

*Figure 31 – colormap used for coloring lines between gridpoints according to their length. The middle green color is used for the equilibrium state of the first frame, so that an increase in length has the color shifted to yellow, orange and red and a decrease in length will shift the color to the blue region.*

When inserting a needle, one can also see the line position vary and the distance between lines increase in some areas and decrease in other, but for the measurements to be significant, the needle must be inserted perpendicularly to the lines' direction.

The lines are saved in image files, each file corresponding to a different frame, so that one can see the evolution of the local line sizes, which translate different compressions, different reactions to the applied forces in different places of the same phantom.

Because of eventual misplacements in the gridpoint centroids, motivated by the errors explained in the previous subsection, also the lines can have sizes that are not correspondent to reality, it is, they may translate a compression that did not happen because their size gets erroneously shortened, and vice versa.

Adding more gridlines to a phantom, which means adding more gridpoints to a 2D image, increases the precision with which the deformation measurements are carried. Granularity was only increased to a maximal grid of 5 lines and 10 columns of gridpoints, which can only be seen to the whole extension in the Siemens Acuson s3000 machine, using a High Definition probe. This is problematic since the image acquired with this machine and probe has overall less quality than the one acquired with Siemens Acuson p500.

After acquiring the differently colored lines that connect gridpoints, an interpolation in the horizontal and vertical direction between lines can be done.

This interpolation allows to have a more global perception of the deformations in the phantom. As two parallel horizontal lines and two parallel vertical lines in the same neighborhood form a square with differently colored edges, the color gradient between the horizontal lines allows for the perception that one horizontal plane of the phantom was more compressed than another, since more compression corresponds to a different color. The same happens for the vertical lines: they can acquire different lengths throughout the phantom and a color gradient between them allows for the identification of places in which there is more compression (since these lines are parallel to the applied force, they stretch more as the compression increases).

These two interpolations are averaged for all the points in the squares formed by each two pairs of parallel lines.

### 3) *Elastography*

#### a) *Ground truth for elastography through compression tests*

To know if the values of Young's Moduli calculated by the developed algorithm are coherent with the reality, a reference method of elastography was used. This method consisted of applying the same forces (the same weights) on the phantoms through the same method as in the algorithm to be described below. A thin acrylic plate was placed under each weight to make sure that the force was being applied thoroughly on the whole surface of the phantom.

The strains were measured with a digital caliper rule with sub-millimeter precision, between either two vertically consecutive gridpoints or the upper and bottom surface of the phantom (**figure 32**). This second method created better results in terms of variance and Coefficient of Determination in the calculated linear regression because the distance between points decreases in very small portions with the compressions applied, and its measurement is more subject to operator error.

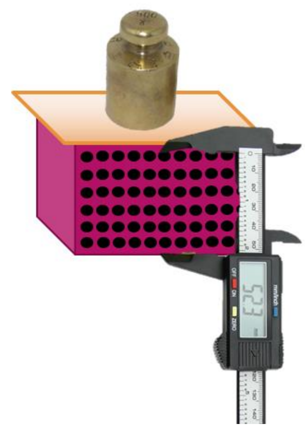

*Figure 32 – setup for measuring the Young's Modulus through compression tests, that involves placing weights on top of an acrylic plate (orange) and measuring the deformation of the phantom with a caliper rule*

#### b) *Local Young's Moduli calculation algorithm*

It is possible to measure the local Young's Moduli in the phantom in the regions where the horizontal deformations are measured, since the lines between horizontally placed gridpoints shorten proportionally to the compression done on the surface of the phantom. This is because these horizontal deformation measurements are in the same direction as the applied compression force, and, if the applied force can be placed under the elastic limit of the material, above which the material has a plastic behavior, the relation between the stress (compressive) and the strain is linear, given by the Young's Modulus in a specific line between two points.

The global Young's Modulus of a phantom can be calculated through these local measurements, considering the example of a homogeneous phantom, in which (in an ideal case), all the horizontal strains should be similar for a certain applied stress. The stress needs to be equally distributed through the surface of the phantom, so that it is the same in every gridpoint. For this, a thin plate is placed over the phantom, and the weight is placed above it (**figure 33**)

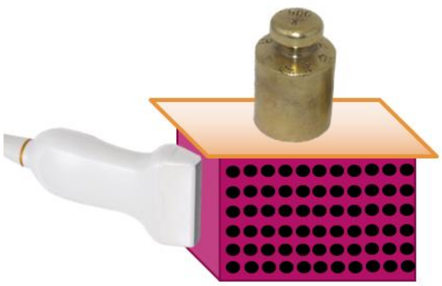

*Figure 33 – placement of the probe and weight in relation to the phantom. In orange, the representation of the acrylic plate on top of the phantom.*

This simplistic approach follows the physics background of Hooke's Law, in which the Young's Modulus is the proportionality factor. In Hooke's Law, the elongation of a massless spring is proportional of the tensile stress applied in it.

The phantoms are considered massless springs for simplification of calculi, even though they are not massless, and that there is friction between the phantom and the probe and the phantom and the table where it stands. The bottom part of the phantom does not deform (expand) laterally in the same way as upper horizontal sections because its lateral expansion is stopped by the friction between this bottom section and the table.

Taking this simplification in consideration, the expression for the Young's Modulus calculation is given by **equation 1**. It expresses that, knowing the displacement between nodes (gridpoints), $\varepsilon$, the force exerted in the phantom's surfaces and the surface, F, and the surface area of the phantom, A, the Young's Modulus, E, can be calculated. The displacement between nodes is calculated as the fraction between the difference between initial length of a line (in equilibrium) and its length when a certain force is applied ($\Delta L$), and the initial length of this line ($L_0$).

$$E \equiv \frac{\sigma(\varepsilon)}{\varepsilon} = \frac{F/A}{\Delta L/L_0} = \frac{FL_0}{A\Delta L}$$

*Equation 1 – expression for the calculation of the Young's Modulus*

A protocol must be followed so that the stresses applied, and measured strains, can be correlated in the ultrasound videos: the probe must be fixed on the side of a phantom and a considerable amount of ultrasound gel must form the interface between the probe and the phantom.

The first five seconds of the video should present the phantom with no additional weight placed on it, except for the acrylic plate. This part of the video will represent the equilibrium state, in which the initial lengths, $L_0$, will be measured.

In the second five seconds, following the first protocol, a weight of 200g would be placed on top of the plate. In the third five seconds, one would prepare a weight of 500g, so that it would be placed and balanced correctly on the phantom in the fourth five seconds. In the fifth five seconds, one should remove the 500g weight and place 1000g over the plate, so that in the sixth five seconds, the equilibrium is already reached with this weight. This being said, the protocol 1 for Young's Modulus calculation would require 30 seconds of video to be concluded. For each five seconds in which the phantom is in equilibrium (with or without weights on top), one second would be considered and the displacements in this second acquired for further processing and calculations.

Because this succession of weight placements in protocol 1 didn't create displacements of points large enough to be clearly visible in the ultrasound videos, protocol 2 was created. This protocol requires 40 seconds, since the placed weights are 500g, 1000g, 1500g (a weight of 1000g plus one of 500g) and 2000g (two weights of 1000g). The placements of these weights and the measurements in the equilibrium state require eights slots of five seconds.

To calculate the stresses, which are the applied pressures, the forces applied by these weights are divided by the area of the phantom surface. The strains are relative measures of distances, so the unit of calculation of distance between points is not relevant. The Young's Modulus is acquired through a linear regression, either for the whole phantom, considering that it is homogeneous, or for each line, locally. Then, these local Young's Moduli can be combined through an average weighted by the coefficient of determination ($R^2$) for the linear regression for each line. This means that the products between the Young's Moduli and the Coefficients of Determination for each line, for the lines in which the Coefficients of Determination are positive, are summed and divided by the sum of all the considered Coefficients of Determination.

The latter method provides with the best results because only the Young's Moduli that are calculated with an acceptable linear regression (a negative $R^2$ means that a horizontal line would fit better to the data than the calculated regression) are considered, and because the values of Young's Modulus with a bigger $R^2$ have more preponderance on the final result.

The results of local Young's Moduli are presented numerically, written over the location of the lines that originated them in an image of the analyzed video, or presented more intuitively as colors, ranging from blue to red, also placed in the line site.

For the Young's Moduli results, a colormap was designed so that there could be an emphasis in results for values below half of the scale. This is done because the Young's Moduli are mostly situated below 50 kPa (around 0.4 in the scale, since the values for the Young's Moduli, in kPa, are divided by 120) for the results seen in the phantoms used in this project (**figure 34).** This colormap has a region of high contrast in the lower values for this reason. It was created by adjusting a regular *jet* colormap with 64 color bins.

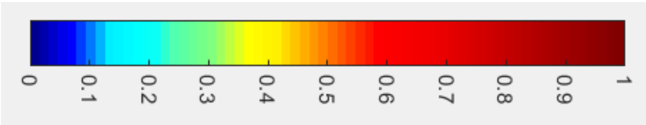


*Figure 34 – colormap for representation of the local Young's Moduli in the image places where they are measured. The region with higher color contrast is located under 0.5 because the scale is prepared to show the more prevalent values with more contrast.*

## IV. Results

### *1) Phantom fabrication*

The final phantoms, used in most of the result acquisition, were done using the final methods described in the section III. The gridlines that proved to be more efficient were the ones made of fishing line. Lines made of PVC with silica gel were not efficient, since the silica gel would spread to the surroundings and the property of having echogenic lines over an anechoic background would be compromised.

The creation of a 3D-printed box with holes as a phantom mold added more reproducibility to the process of phantom fabrication and allowed for the results in phantoms with different stiffness properties to be comparable.

It was useful to create parallelepipedal phantoms, instead of breast shaped ones, even though they don't simulate the constraints that the real shape of the breast implies. The more complex the phantom shape is, the more difficult it is for the air bubbles to be completely released.

As for the methods for gridline placement inside the phantom, the first method attempted, besides being more time consuming, because it required that several parallel lines would be "sewed" inside a piece of solid PVC, places the lines in positions that would be less precise than when the lines are already placed, before the PVC is poured. This technique would be more dependent on the proficiency of the person fabricating the phantom, therefore, allowing for less reproducibility. Creating a mold with holes for previous positioning of the lines, instead of inserting them after the phantom solidifies creates visibly better results.

A homogeneous phantom was done with 70% PVC and 30% plasticizer (**figure 35**). Its largest surface had an 8 cm by 8 cm area and it was 4,5 cm tall.

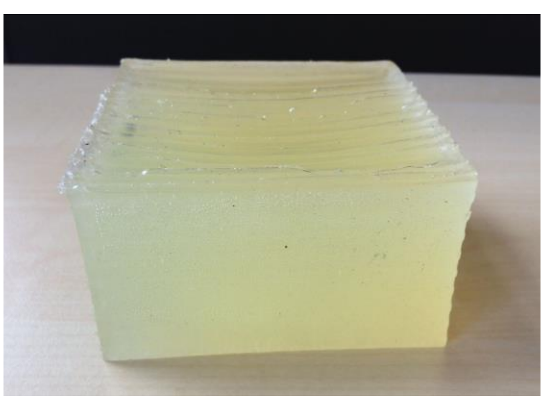

*Figure 35 – homogenous phantom. The upper surface gridlines can be seen on top of it.*

A biphasic phantom, with a stiff region and a softer region was fabricated (**figure 36**). The regions are parallel between them and parallel to the gridlines. The stiffer part was made of 85% PVC and 15% plasticizer, and the softer part was made of 75% PVC and 25% plasticizer. Its dimensions are 8 cm by 7 cm, with a height of 3.5 cm.

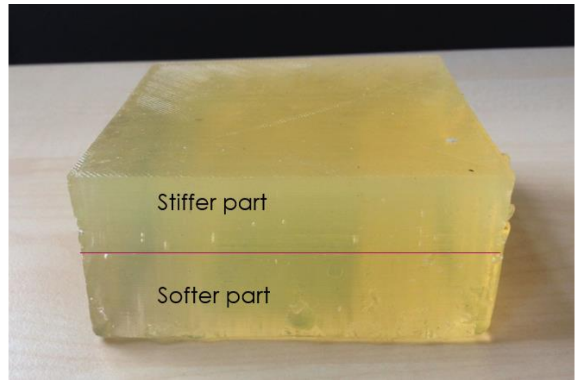


*Figure 36 – biphasic phantom. The stiffer and softer part are signaled, and the lines are displaced parallelly to the pink line.*

A phantom with a small inclusion on the side was done with a bulk of 90% PVC and 10% softener and an inclusion of 90% PVC and 10% hardener (**figure 37**). The dimensions are 8 cm by 7 cm, with a height of 4 cm for the whole phantom, and the lesion is positioned touching one of the borders, away 5.5 cm from the other border. The lesion has a surface of 2 cm by 2.5 cm and a height of 3 cm. There is a layer of 1 cm of the same composition as the lesion in one of the larger surfaces of the phantom.

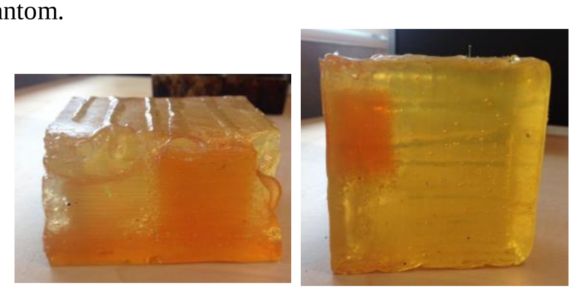

*Figure 37 – side view and upper surface view of the phantom that has a small stiff inclusion. The darker orange region corresponds to stiffer PVC.*

A phantom with a larger, central lesion (**figure 38**), was done with a bulk of 90% PVC, 10% softener, and an inclusion of 90% PVC and 10% hardener. The dimensions are 6.5 cm by 7.5 cm for the largest surface of the whole phantom, which has a height of 4 cm. The lesion has a surface area of 3.5 cm by 3 cm and a height of 1.5 cm. 1 cm of the height of the whole phantom is made of lesion material, in which the lesion stands.

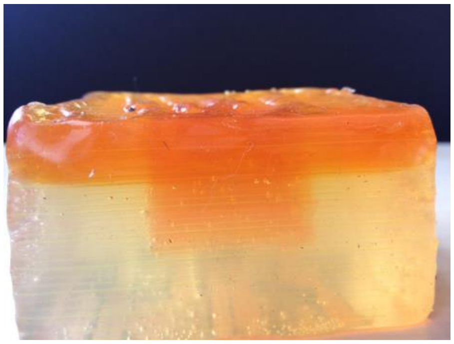

*Figure 28 – phantom with a central lesion. The darker, orange regions correspond to the stiffer material.*

*2) Deformation quantification*

*a) Deformations with external compression*

When no compression is applied to the phantom, the distances between the points are considered as the reference, so they are colored equally in green, which is the color in the middle of the full scale. The distances between gridpoints for a 2D plane of a plane in which 5 lines and 6 columns of lines are considered, when no compression is applied, can be seen in **figure 39.**

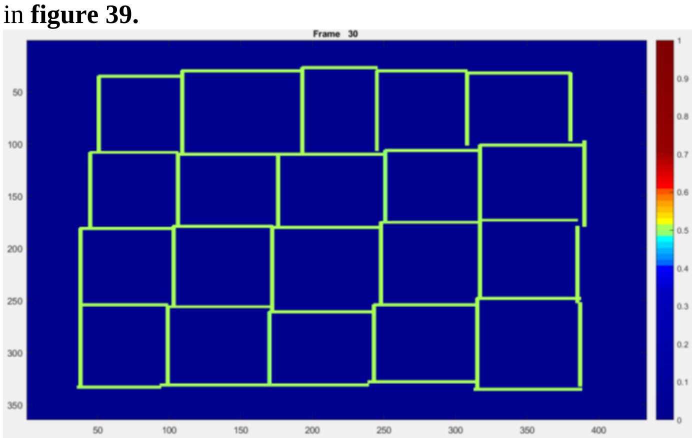


*Figure 39 – lines between gridpoints when no compression is being applied. All the lines are colored green because the distance between the points corresponds to the equilibrium state.*

When equal compression is being applied to all the points the part of the phantom represented on the right, in this case, the largest surface of the phantom, the horizontal lines start to shorten, shifting to lower color levels in the scale, going from green to light blue, and the vertical lines start to stretch, since they are parallel to the direction of the force application, shifting to higher color levels, going from green to yellow. This can be seen in **figure 40.**

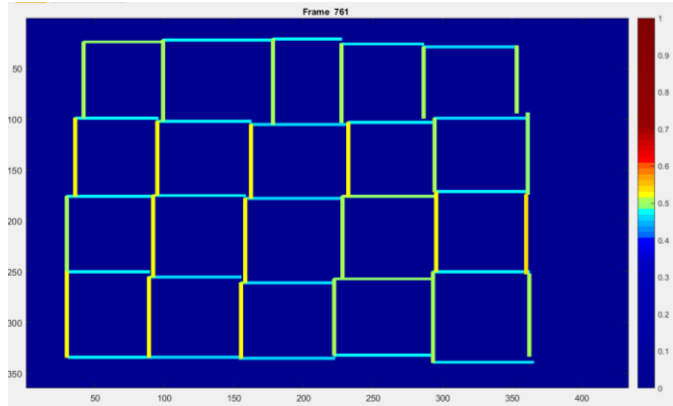


*Figure 40 – lines between gridpoints when a compression is done on the right side, with a weight of 1500 g over the largest surface of the phantom. The horizontal lines are colored in light blue because they are shortened, and, because the distance between points, vertically, increases, some of the vertical lines are colored yellow.*

For the interpolation between the line colors, presented on **figure 41**, one can observe the evolution from the equilibrium state, in which no pressure is being applied on the phantom (the pressure is applied on the right side, the upper surface of the phantom; the image is always tilted 90 degrees to the right relatively to the position of the phantom above a table), in which the lines are equally colored, to the compression state in which a weight of 1500 g is placed on top of the phantom, and the compression state in which a weight of 2000g is used.

The second, third and fourth images are heterogeneous in color, showing that the lines don't behave ideally: given a constant pressure, they don't deform in the same ratio relatively to the equilibrium state. Still, it is possible to observe a general change in color when the successive compressions are done.

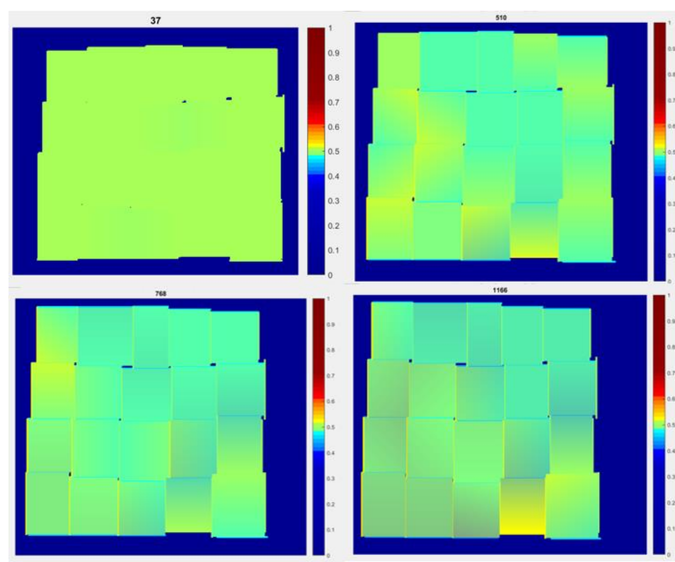


*Figure 41 – interpolation of the color values in the vertical and horizontal direction for a compression of a homogeneous phantom. The first image shows the equilibrium state, no weight placed on top of the phantom. The second shows the compression of the phantom with a weight of 1000 g and the third shows an increase of 500 g to the previous one. The fourth image shows the compression of the phantom with 2000 g.*

The interpolations in the horizontal direction and vertical direction alone can be analyzed individually. In the same scenario and video as for **figure 41**, the interpolation in both directions, the horizontal interpolation shows only how the lines parallel to the surface in which the force is being applied (on the right), perpendicular to the force itself, stretch, being its increase in length translated by a shift to yellow and orange values in the colormap (**figure 42**). The vertical interpolation shows the shortening of the lines that are parallel to the direction of the force and a shift to darker blue colors can be seen (**figure 43**).

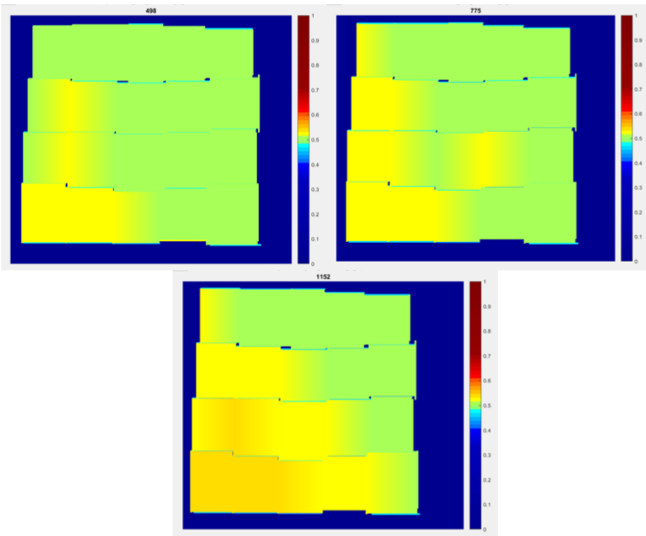

*Figure 42 – horizontal interpolation of the color values for a compression of a homogeneous phantom. The first picture shows the compression of the phantom with a weight of 1000 g. The second shows the compression with 1500 g and the third one with 2000 g.*

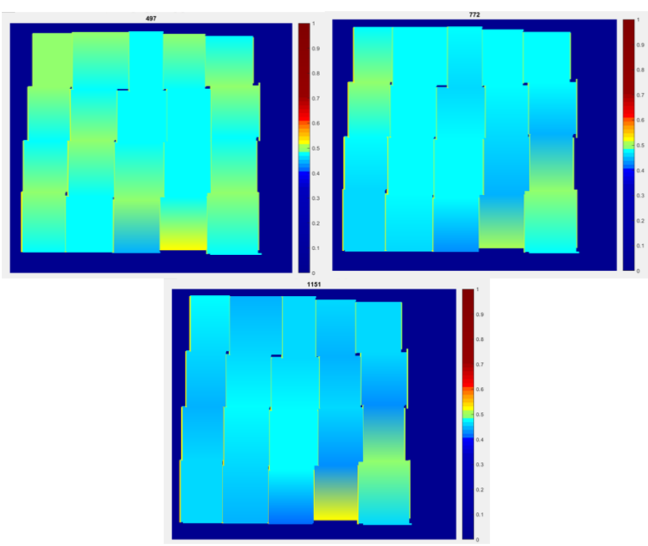

*Figure 43 – vertical interpolation of the color values for a compression of a homogeneous phantom. The first picture shows the compression of the phantom with a weight of 1000 g. The second shows the compression with 1500 g and the third one with 2000 g.*

*b) Deformations with needle insertion*

Needle insertions produce different displacements of gridpoints in different parts of the 2D section of the phantom as they are being performed. In **figure 45**, the two-way interpolation of the point distance related colors shows the chronologically ordered results for the same frames in the **figure 44.**

In this case, the needle insertion plane is slightly deviated from the imaging plane, so the needle can only be seen on the right border of the image, and the echogenic point that it creates is not detected by the algorithm. If the needle is inserted exactly in the same plane that the probe is analyzing, it will create a shadowing artifact, not allowing for the points that are affected by it to be correctly traced.

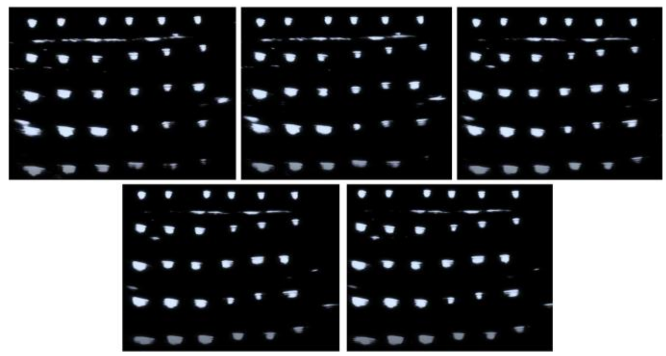

*Figure 44 – 4 frames of a needle insertion video, chronologically ordered. The line artifact between the first and second lines is caused by a previous needle insertion: it is a trace of air. The needle is inserted between the third and the fourth lines.*

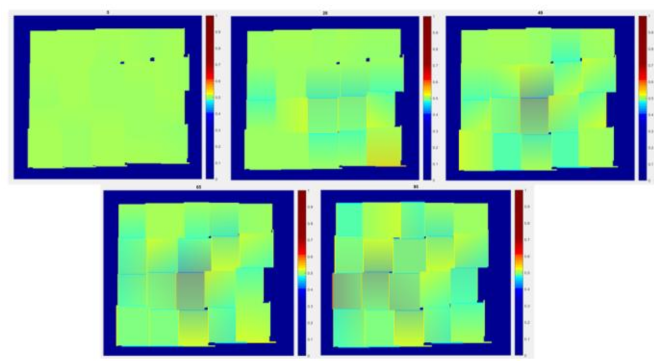

*Figure 45 – the same frames of needle insertion as in figure 44, processed in terms of distance between points and of color interpolation. One can see, through the darker areas that are being generated from image to image, the movement of the needle, from the right to the left, in the third line of squares formed by color interpolation.*

### 3) *Elastography*

*a) Results for different phantoms*

For a homogeneous phantom, with a surface area of 8 cm by 8 cm and a height of 4.5 cm, the acquired global Young's Modulus with the compression test, through the data of the **figure 46**, is different when acquired through the data of the **figure 47**. This is because the first was calculated measuring distances between gridlines and the second measuring the global compression of the phantom, the distance between the upper and the bottom surface for each applied force.

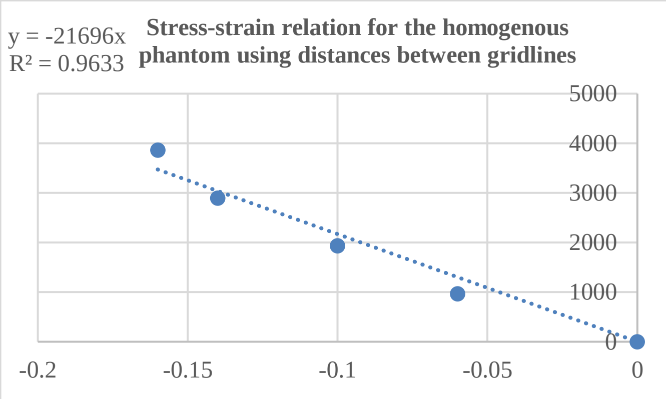


*Figure 46 – Stress-strain relation for the homogeneous phantom obtained by a compression test using distances between gridlines. The resultant Young's Modulus is of 21,70 kPa*

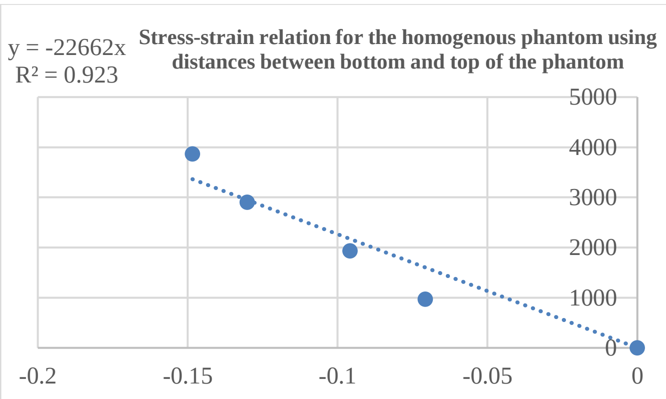


*Figure 47 – Stress-strain relation for the homogeneous phantom obtained by a compression test using distances between the bottom and top of the phantom. The resultant Young's Modulus is of 22,66 kPa*

As for the calculations of the moduli using the proposed algorithm, the results are also different when calculated with all the points or as the weighted average of the local values.

Also, scanning the phantom from the largest surface, placing the weight on the side surface (smaller area), and scanning the phantom from the side, produces different results. Scanning the phantom from the largest surface allows for the tracking of a bigger amount of points than the same scan on the side, since scanning the phantom on the side does not occupy the whole extension of the probe, but only about two thirds of it. On the other hand, scanning the phantom from the largest surface implies placing the weights in a more unstable manner, since the surface of the phantom that is placed on the table is the one with the smallest area. On **figure 48,** one can see the local Young's Moduli calculated through scanning on the largest surface, placing weights according to the protocol 1.

The global Young's Modulus calculated through considering all the distances for each weight is 23.75 kPa, and the linear regression that originated this value is associated with $R^2$=0.64. Calculating a weighted average of the local Young's Moduli, leaving out the results associated with a negative $R^2$, the obtained value for the global Young's Modulus is 28.98 kPa. 120 frames are used to calculate both results.

In some cases, not all the extracted frames are considered in the calculations, because if a frame lacks the presence of a certain gridpoint, it will affect the existence of one or several lines. For the local Young's Moduli affected by these lost gridpoints not to be calculated with less points than the remaining ones, the frames that don't have the right number of gridpoints (in this case 5 by 7) are left out of the calculations.

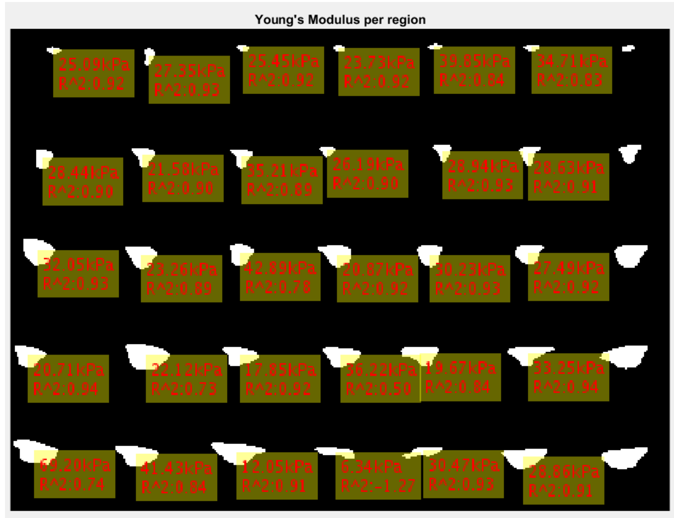


*Figure 48 – local Young's Modulus acquired for a homogeneous phantom, scanning it from the largest surface. The Young's Modulus values are placed in the space where the lines that originated them were traced, between two horizontally adjacent gridpoints, and the $R^2$ associated to each one of them is also presented.*

There is variability of results between different videos for the same phantom since the probe position may not be the same. It can be seen for the following results, acquired on the surface of the homogeneous phantom, following the same methodologies as for the previously presented case: a global Young's Modulus of 23.56 kPa, associated to $R^2$=0.63 when considering all the points and E=29.17 kPa when a weighted average is calculated. The standard deviation between the Young's Moduli considered for the weighted average is of 9.51 and the average $R^2$ is 0.87. Also for this case, 120 frames were used.

The variability increases when one compares the results obtained with the scans on the largest surface and the side scans, with the same protocol. Results for a side scan can be seen in **figure 49**, which only shows a 5 by 6 grid given the height of the phantom only allowing for this grid size. The global Young's Modulus calculated for all the points is 22.71 kPa, associated to $R^2$=0.47, and the one calculated through a weighted average of the local Young's Moduli is of 26.43 kPa. The standard deviation of the Young's Moduli is bigger for this case, being of 10.81, and the average $R^2$ for local measurements is smaller, of 0.73. For this case, 175 frames were used for the calculations, and the introduction of more frames can create more error in the linear regressions.

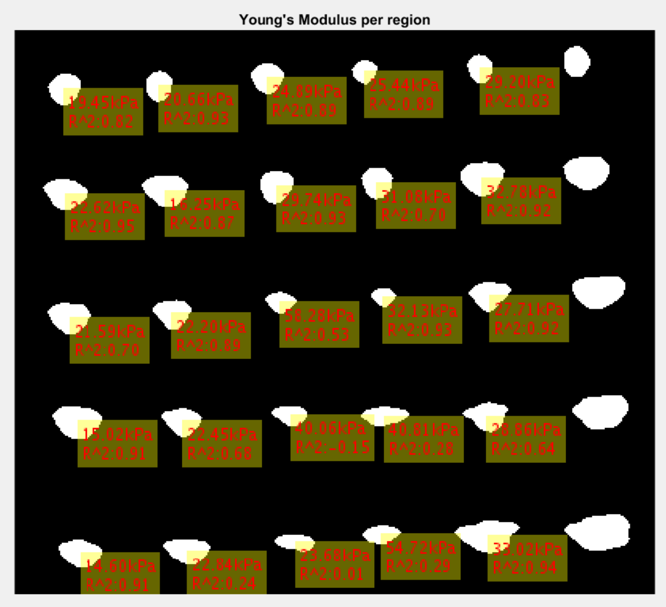


*Figure 49 – local Young's Modulus acquired for a homogeneous phantom, scanning it from the side surface.*

More results for the homogeneous phantom are presented in the table of the **figure 50**, which allows for the comparison between methods for Young's Modulus calculation. The values present in the global Young's Modulus column refer to the Young's Moduli calculated as a weighted average between the local ones, since this is the technique that induces less error in the calculations.

| Mode of acquisition | **Global** Young's Modulus (**kPa**) | Young's Moduli Standard Deviation | $R^2$ average **(for the considered measurements - $R^2$ >0)** | Number of frames **considered** |
|---|---|---|---|---|
| Acuson p500, protocol 1, 5x6 grid, side scan | 19,63 | 8,37 | 0,71 | 120 |
| Acuson p500, protocol 1, 5x7 grid, upper surface scan | 28,98 | 10,47 | 0,87 | 120 |
| Acuson p500, protocol 1, 5x7 grid, upper surface scan | 29,17 | 10,95 | 0,88 | 120 |
| Acuson p500, protocol 1, 5x7 grid, upper surface scan | 28,35 | 8,60 | 0,83 | 120 |
| Acuson p500, protocol 2, 5x6 grid, side scan | 20,74 | 6,34 | 0,86 | 175 |
| Acuson p500, protocol 2, 5x6 grid, side scan | 26,43 | 10,8 | 0,73 | 175 |
| Acuson s3000, protocol 2, 5x6 grid, side scan | 31,38 | 6,73 | 0.74 | 155 |
| Acuson s3000, protocol 2, 5x7 grid, side scan | 32,68 | 7,47 | 0,76 | 155 |

*Figure 50 – table for elastography results of the homogeneous phantom. In the first column, the mode of acquisition informs about which ultrasound machine was used for the video acquisition, which weight placement protocol was followed (either 1 or 2), which grid shape was considered (number of lines x number of columns), and what type of scan was done (on the upper surface or on the side). The second column presents the global Young's Modulus of the phantom calculated through the weighted average of the local values for which the $R^2$ is positive.*

Combining the best results for each local Young's Modulus, it is, taking all the videos obtained from the same 2D section of the phantom, which contain the same gridpoints, but different modes of acquisition, we get a Young's Modulus of 23.61 kPa and an average $R^2$ value of 0.91. Even though the measurements presented in the table can deviate considerably from the reference values acquired by compression tests, the acquisition of several videos and obtention of the best results in terms of $R^2$ for each video seems to produce results that agree better with the reference values. Also, the videos that produce generally best results are the ones done with protocol 2, Siemens Acuson p500, a side scan and a 5 by 6 grid.

The best combination of results can be found in **figure 51**.

| | | | | |
|---|---|---|---|---|
| E=15,10 kPa<br>R^2=0.96 | E=17,99 kPa<br>R^2=0.94 | E=18,7 kPa<br>R^2=0.96 | E=19,92 kPa<br>R^2=0.94 | E=18,1 kPa<br>R^2=0.89 |
| E=33,52 kPa<br>R^2=0.94 | E=15,73 kPa<br>R^2=0.95 | E=24,21 kPa<br>R^2=0.93 | E=19,7 kPa<br>R^2=0.95 | E=30,1 kPa<br>R^2=0.87 |
| E=32,86 kPa<br>R^2=0.94 | E=28,35 kPa<br>R^2=0.96 | E=33,08 kPa<br>R^2=0.85 | E=22.17 kPa<br>R^2=0.94 | E=23,27 kPa<br>R^2=0.88 |
| E=27,10 kPa<br>R^2=0.87 | E=24,02 kPa<br>R^2=0.88 | E=33,75 kPa<br>R^2=0.90 | E=21,51 kPa<br>R^2=0.9o | E=18,87 kPa<br>R^2=0.89 |
| E=23,36 kPa<br>R^2=0.95 | E=39,86 kPa<br>R^2=0.92 | E=24,00 kPa<br>R^2=0.7 | E=28,04 kPa<br>R^2=0.93 | E=26,79 kPa<br>R^2=0.81 |

*Figure 51 – best combination of results for a homogeneous phantom, considering the Young's Modulus values for the best $R^2$ for each line between two gridpoints. This combination of results gives rise to an average global Young's Modulus of 23.61 kPa and an average $R^2$ of 0.91.*

For a phantom with a small inclusion of stiffer PVC, the videos acquired from side scans could only get a view either of the lesion site, because it was situated on the phantom side limit, or of the softer bulk of the phantom. This happens because a video made from the side opposite to the site of the lesion wouldn't possibly be made in such a way that it would picture the bulk of the phantom and the lesion together: the ultrasound video analysis is optimized for a depth of a maximum of 3.5 cm. The lesion, being only 2 cm wide, wouldn't possibly be viewed from the opposite side of the phantom.

This being said, the analysis was made separately for the lesion site and for the soft phantom bulk ultrasound videos. The results of the compression tests for the lesion in this phantom show a global Young's Modulus for this region of 41.75 kPa, associated with $R^2$ = 0.96. The linear regression for these results is in the **figure 52**.

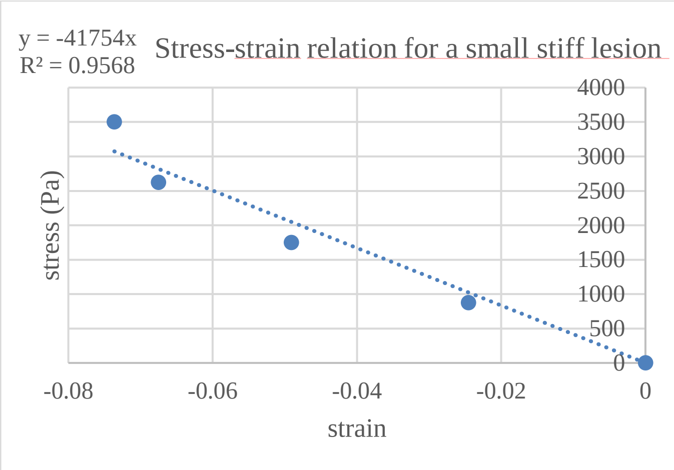


*Figure 52 – Stress-strain relation for the stiff inclusion/lesion embedded in a soft phantom obtained by a compression test using distances between the bottom and top of the lesion. The resultant Young's Modulus is of 41.75 kPa*

The results for the compression tests in the softer part of the phantom show a global Young's Modulus of 17.81 kPa, associated to $R^2 = 0.96$. The linear regression for these results can be seen in **figure 53**.

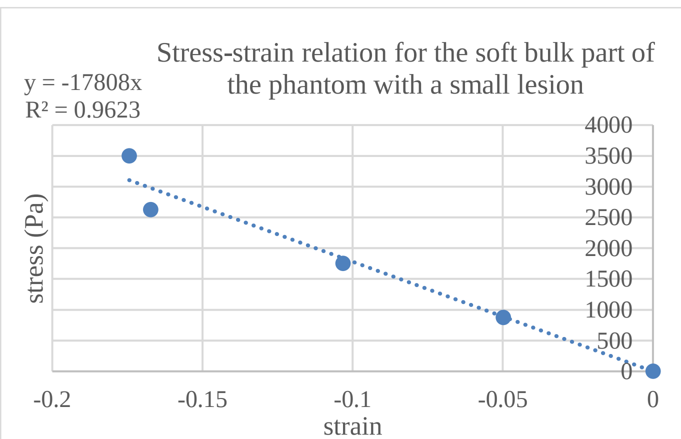


*Figure 53 – Stress-strain relation for the soft region of the phantom which has a small inclusion on one side, obtained by a compression test using distances between the bottom and top of the phantom, in the side in which the lesion is not present. The resultant Young's Modulus is of 17.81 kPa*

This phantom was analyzed with Siemens Acuson p500, using a 5 by 6 grid for each video, using protocol 2.

For the videos that only show the inclusion part, the stiffer region of the phantom, the global Young's Modulus obtained with all the points had a value of 31.52 kPa, associated with $R^2 = 0.34$, and, for another video, a modulus of 35.57 kPa, associated with $R^2 = 0.26$. For the weighted average of the local Young's Modulus, the results obtained were, respectively, 41.064 kPa, for the first video, using 160 frames, and 47.33 kPa for the second, using 170 frames.

A combination of the best results for the two videos, in terms of $R^2$, is presented in **figure 54,** and it shows a global Young's Modulus of 40.39 kPa associated to $R^2$ =0.88.

The latter results, combining two different videos, can achieve a Young's Modulus that only differs from the reference one by 1.36 kPa.

Nevertheless, the standard deviation between the local Young's Moduli is of 16.53, a considerably big value for a region of the phantom that is supposed to be homogeneous. The average $R^2$ is of 0.88 for the local Young's Modulus that are included in this combination.

| | | | | |
|---|---|---|---|---|
| E=66,97 kPa R^2=0,88 | E=53,99 kPa R^2=0,83 | Negative R^2 | E=33,05 kPa R^2=0,90 | E=33,18 kPa R^2=0,54 |
| E=55,92 kPa R^2=0,89 | E=43,89 kPa R^2=0,87 | E=87,86 kPa R^2=0,85 | E=30,96 kPa R^2=0,91 | E=23,96 kPa R^2=0,96 |
| E=53,65 kPa R^2=0,92 | E=62,94 kPa R^2=0,90 | E=51,22 kPa R^2=0,89 | E=27,11 kPa R^2=0,96 | E=27,08 kPa R^2=0,94 |
| E=47,85 kPa R^2=0,87 | E=36,00 kPa R^2=0,92 | E=31,45 kPa R^2=0,93 | E=33,60 kPa R^2=0,97 | E=23,44 kPa R^2=0,96 |
| E=20,67 kPa R^2=0,95 | E=38,25 kPa R^2=0,79 | E=39,71 kPa R^2=0,78 | E=23,42 kPa R^2=0,96 | E=30,69 kPa R^2=0,83 |

*Figure 54 – best combination of results for the stiff region in a phantom with an inclusion/lesion, considering the Young's Modulus values for the best $R^2$ for each line between two gridpoints, for two videos done with the same methods. This combination of results gives rise to an average global Young's Modulus of 40.39 kPa and an average $R^2$ of 0.88.*

The same method of analysis was used for the soft part of the phantom, by means of two videos to get the best combination of results.

The two videos, alone, had the following results: The Young's Modulus of the first one, calculated using all the points, was of 18.487 kPa, associated to an $R^2$ of 0.53. Even though this value is close to the one obtained for the reference, the one obtained through a weighted average of local moduli is of 23.07 kPa. For the latter calculation, the standard deviation of the local moduli is of 8.87 and the average $R^2$ is of 0.87. For the second video, the values get even more deviated from the reference, with a global Young's Modulus calculated with all the points of 26.02 kPa, associated with an $R^2$ of 0.51, and the modulus acquired by a weighted average with a value of 31.80 kPa, being the standard deviation of the local values of 11.78 and the average $R^2$ of 0.82. For this video, 155 frames were used in the calculations.

The best combination of the values in the two videos produces a Young's Modulus, calculated by a weighted average of the local ones, of 26.44 kPa, associated with a $R^2$ of 0.93. The combination table can be seen in **figure 55**.

| | | | | |
|---|---|---|---|---|
| E=19,9 kPa R^2=0,92 | E=34,26 kPa R^2=0,94 | E=35,41 kPa R^2=0,87 | E=22,59 kPa R^2=0,94 | E=23,96 kPa R^2=0,96 |
| E=14,29 kPa R^2=0,92 | E=36,63 kPa R^2=0,95 | E=11,98 kPa R^2=0,83 | E=30,46 kPa R^2=0,93 | E=13,56 kPa R^2=0,95 |
| E=25,27 kPa R^2=0,90 | E=27,75 kPa R^2=0,92 | E=17,42 kPa R^2=0,95 | E=23,55 kPa R^2=0,96 | E=15,63 kPa R^2=0,96 |
| E=49,86 kPa R^2=0,85 | E=33,5 kPa R^2=0,95 | E=25,91 kPa R^2=0,94 | E=23,68 kPa R^2=0,96 | E=19,41 kPa R^2=0,95 |
| E=46,08 kPa R^2=0,86 | E=19,89 kPa R^2=0,95 | E=31,17 kPa R^2=0,95 | E=30,49 kPa R^2=0,92 | E=31,82 kPa R^2=0,90 |

*Figure 55 – best combination of results for the soft bulk region in a phantom with an inclusion/lesion, considering the Young's Modulus values for the best $R^2$ for each line between two gridpoints, for two videos done with the same methods. This combination of results gives rise to an average global Young's Modulus of 26.44 kPa and an average $R^2$ of 0.93.*

The difference between the Young's Modulus of the best result combination, 26.44 kPa, and the one acquired through compression tests, for the same area, 17.81 kPa, may be motivated by the presence of the stiffer lesion in the phantom, which may act as a pivot when the weights are placed over the phantom, in the ultrasound imaging process. This stiffer region may prevent the surrounding softer regions from deforming in the same way as the regions further from the lesion, creating less deformation for the same stress in some regions, increasing the global Young's Modulus obtained by ultrasound imaging.

**Figure 56** shows the color representation of the softer region of the phantom, and under it, the actual values that correspond to the represented colors of the upper image. Even though the colors seem to identify a homogeneous phantom, in terms of elasticity, on the lower left corner, the Young's Modulus appears to be much higher than for the rest of the represented sites. This specific result, as can be seen in the lower image of figure x, also corresponds to the value calculated with the higher error in this process, being associated with a negative Coefficient of Determination.

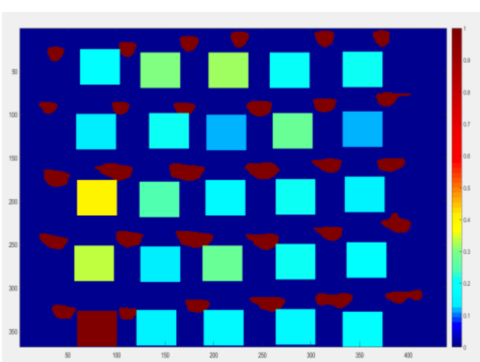

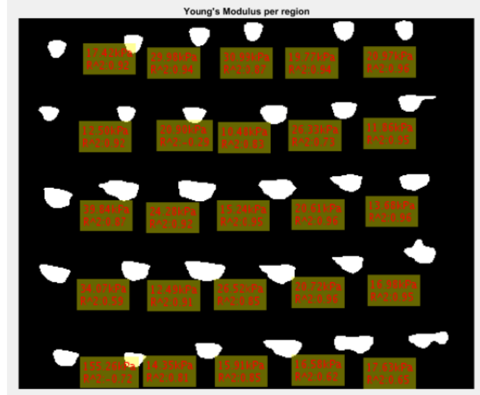


*Figure 56 – the upper image has the color representation of the local Young's Moduli, which are specified in the lower image, for the soft part of the phantom with a small stiff inclusion, which is not seen in this result.*

To overcome the visualization problems encountered in the previous phantom, for which the videos could only be done either with the stiffer or the softer zone, and not a mix of both, a phantom with a central lesion, standing on one of the largest surfaces but visible in a radius of 3 cm from both sides, was used.

Two videos of the phantom were done, in which the lesion could be seen in some of the gridpoints placed on the lower left part.

The results of the compression tests, in which the soft bulk of the phantom and the lesion are analyzed individually, can be seen in the **figures 52 and 53.** The materials used for this phantom are the same as for the previous one, only the relative disposition of the soft bulk and lesion are different between the two phantoms. So, it is expected for the lesion site to have a Young's Modulus of approximately 41.75 kPa and for the bulk to have a Young's Modulus of 17.81 kPa.

Because this phantom is taller than the previous one, a grid of 5 lines by 7 columns could be considered for the measurements. The resultant local Young's Moduli can be seen in **figure 57**, for one of the videos. The region surrounded is occupied by stiffer PVC.

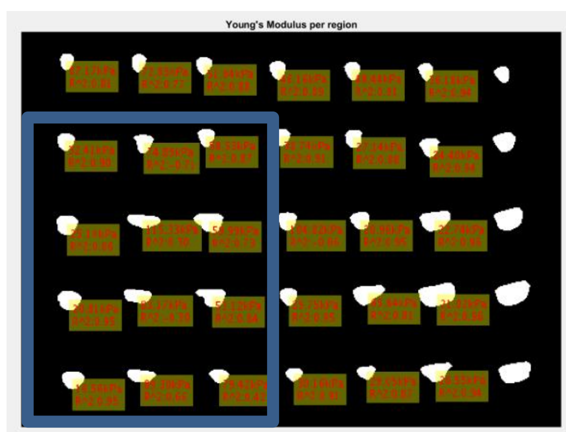


*Figure 57 – Local Young's Moduli for a phantom with a stiffer lesion, which can be seen surrounded by a blue frame. The results presented were obtained with a side scan of the phantom.*

In the same way as for the previous studies, the best results were combined, arriving to an average Young's Modulus of 29.34 kPa for the soft part of the phantom and of 40.34 kPa for the stiff part. The stiff part Young's Modulus is much closer to the refence value of 41.75 kPa than the modulus for the soft part, due to the same reason stated in the last study: the stiffer part of the phantom can create an impediment of movement in the surrounding zones, creating higher Young's Moduli where lower values should be.

Finally, comes the analysis for the biphasic phantom, designed placing a layer of softer PVC over a layer of stiffer PVC, and not including a "lesion".

The compression tests results presented in **figures 58 and 59** suggest a Young's Modulus of 30.03 kPa for the stiffer part, associated with a $R^2$ of 0.99 and a Young's Modulus of 18.21 kPa for the softer part, associated with a $R^2$ of 0.98.

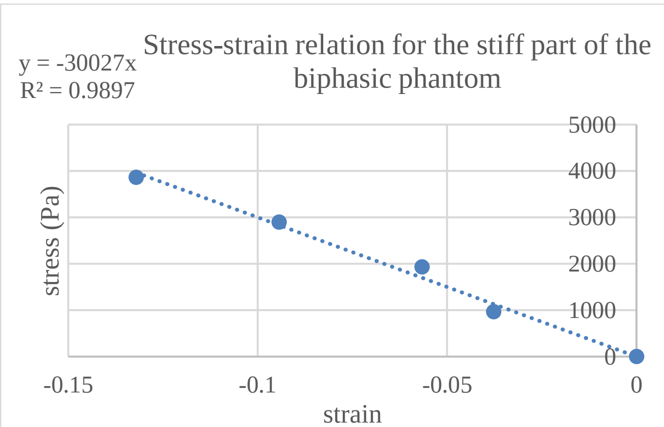


*Figure 58 – Stress-strain relation for the stiff region of the biphasic phantom, obtained by a compression test using distances between the bottom and top of the stiff region. The resultant Young's Modulus is of 30.03 kPa*

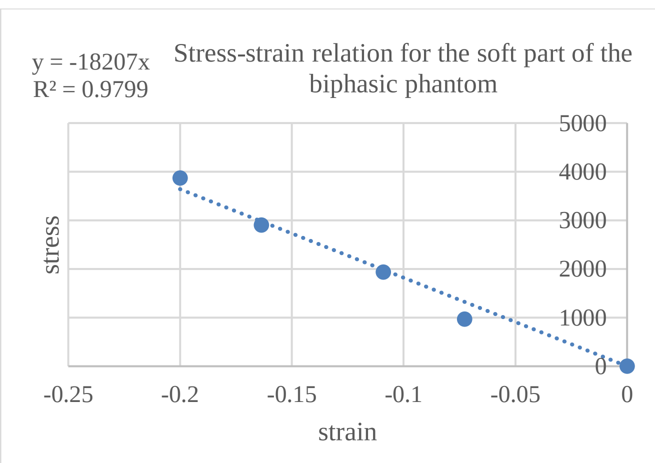


*Figure 59 – Stress-strain relation for the soft region of the biphasic phantom, obtained by a compression test using distances between the bottom and top of the soft region. The resultant Young's Modulus is of 18.21 kPa*

The videos of this phantom vary in acquisition mode and are done with both protocols. They suggest a high variance of results between methods, being some of the results close to the reference ones and others very deviated from it. Nevertheless, a clear distinction between a softer and a stiffer region could be seen when side scans were used. The results would also vary if the weight was applied on the stiffer surface of the phantom or on the softer one.

The results in **figure 60** are for a video done applying the weights on the softer part of the phantom, seen on the right. The zone delimited by blue lines is located on the interface between the stiffer and the softer zones, so it is not considered for the calculations of any of the regions' Young's Modulus.

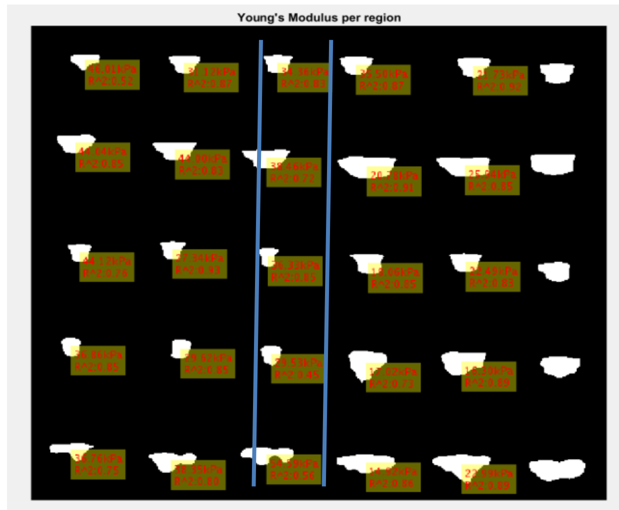


*Figure 60 – results of the local Young's Moduli for the biphasic phantom. On the left of the region limited by the blue lines, the stiffer part of the phantom, with a Young's Modulus calculated by a weighted average of the values in this zone of 37.29 kPa. On the right of the limited region, the softer part of the phantom, with a Young's Modulus of 21.63 kPa.*

The results on **figure 61** are for placing the weights on the stiffer part of the phantom, seen on the right. In the previous case, the results for the softer part would be closer to the reference ones than for this case, in which the results for the stiffer part are closer to the reference. This suggests a correlation between the proximity of the applied weight place to the gridlines to a better estimation of the local Young's Modulus.

The Young's Modulus on the left, softer side of the phantom, for this second video, is of 25.56 kPa, and for the stiffer, right side, of 32.02 kPa.

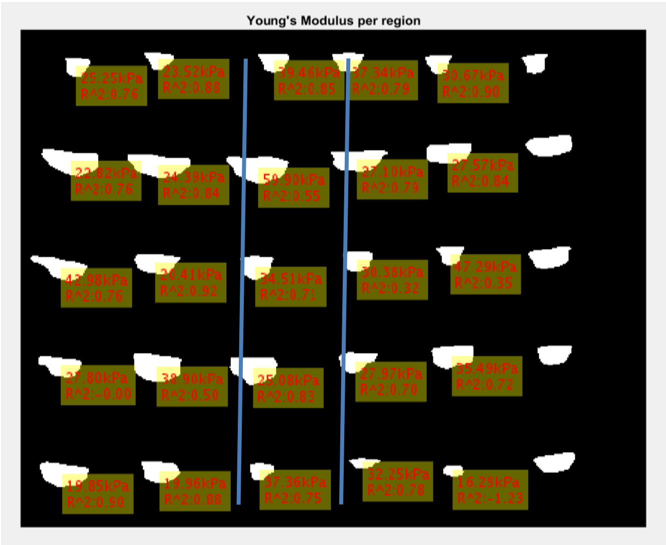


*Figure 61 – results of the local Young's Moduli for the biphasic phantom. On the left of the region limited by the blue lines, the softer part of the phantom, with a Young's Modulus calculated by a weighted average of the values in this zone of 25.56 kPa. On the right of the limited region, the stiffer part of the phantom, with a Young's Modulus of 32.02 kPa.*

Combining the best results of four different videos of the same 2D section of this biphasic phantom, the results improve globally in terms of proximity to the reference, which can be seen in **figure 62**. The Young's Modulus on the stiffer side is 31.76 kPa, and, on the softer side, 23.73 kPa.

| | | | | |
|---|---|---|---|---|
| E=28.97 kPa $R^2$=0.92 | E=27.28 kPa $R^2$=0.94 | E=28.48 kPa $R^2$=0.88 | E=30.86 kPa $R^2$=0.94 | E=23.72 kPa $R^2$=0.94 |
| E=35 kPa $R^2$=0.9 | E=31.46 kPa $R^2$=0.95 | E=37.71 kPa $R^2$=0.95 | E=34.78 kPa $R^2$=0.94 | E=35.72 kPa $R^2$=0.96 |
| E=24.89 kPa $R^2$=0.95 | E=27.34 kPa $R^2$=0.93 | E=35.18 kPa $R^2$=0.94 | E=21.97 kPa $R^2$=0.93 | E=17.75 kPa $R^2$=0.96 |
| E=31.52 kPa $R^2$=0.89 | E=42.42 kPa $R^2$=0.92 | E=41.42 kPa $R^2$=0.79 | E=18.8 kPa $R^2$=0.97 | E=16.01 kPa $R^2$=0.89 |
| E=39.08 kPa $R^2$=0.94 | E=29.61 kPa $R^2$=0.96 | E=34.5 kPa $R^2$=0.91 | E=14.7 kPa $R^2$=0.91 | E=22.99 kPa $R^2$=0.89 |

*Figure 62 – best combination of results for the biphasic phantom, which produces a Young's Modulus of 31.76 kPa for the stiffer part and a Young's Modulus of 23.73 kPa for the softer side.*

A color representation of the local Young's Moduli in the biphasic phantom is presented in **figure 63.**
In this figure, one can see that the right side of the phantom (excluding the central column, which is placed in the soft-stiff interface) is softer than the left side, since lower values of Young's Moduli correspond to the green and blue areas, and higher values have their color shifted to higher values in the scale, so to red and orange tones.

Under the color representation, in **figure 63,** the values for the Young's Moduli can be seen, as well as the correspondent Coefficients of Determination. It can be seen that the blue zones correspond to Young's Moduli around 15 kPa, and that the green zone has values from 20 to 30 kPa. Yellow is lighter in the softer zone, going to more orange tones in the stiffer zone, because in this shifting zone of the colormap, the moduli go to values around 40 kPa. Values in the dark red and brown zone correspond to erroneous acquisitions.

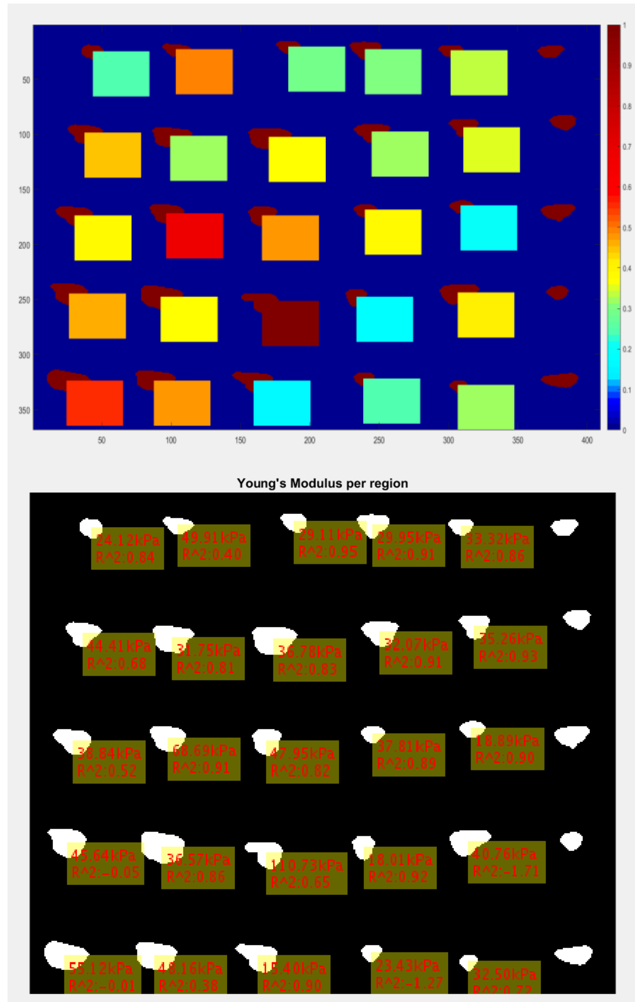


*Figure 63 – color representation of the local Young's Moduli in the biphasic phantom. Under, the numeric values for the moduli and for the $R^2$.*

Picturing the variability between the results acquired by various methods, the table in the **figure 64** shows that the distinguishing between the stiffer and softer part through every method is possible, but that the values acquired may not agree with each other or/and with the references.

| Mode of acquisition | Softer part Young's Modulus (kPa) | Softer part Young's Moduli Standard Deviation | Stiffer part Young's Modulus (kPa) | Stiffer part Young's Moduli Standard Deviation | $R^2$ average (for the considered measurements - $R^2$ >0) | Number of frames considered |
|---|---|---|---|---|---|---|
| Acuson p500, protocol 1, 6x5 grid, side scan | 21,70 | 7,37 | 33,28 | 6,21 | 0,85 | 120 |
| Acuson p500, protocol 1, 6x5 grid, side scan | 21,63 | 5,98 | 37,29 | 6,74 | 0,83 | 120 |
| Acuson p500, protocol 2, 6x5 grid, side scan | 31,45 | 13,38 | 38,07 | 19,18 | 0,88 | 170 |
| Acuson p500, Protocol 2, 6x5 grid, Side scan | 28,10 | 10,25 | 49,45 | 23,37 | 0,35 | 124 |
| Acuson s3000, protocol 2, 7x5 grid, side scan | 29,21 | 10,20 | 33,23 | 21,57 | 0,69 | 155 |

*Figure 64 – table for elastography results in the biphasic phantom. Results acquired for different modes of acquisition, for the softer and stiffer parts of the phantom. The data for the soft part was acquired together with the data for the stiffer part, being that they are visualized in the same image.*

## V. Conclusions

With this project, most of the research questions were answered: it is possible to use ultrasound imaging to quantify deformations and acquire elastography data, using an absolute referential placed in a phantom.

When doing compressions and needle insertions, one can qualitatively observe, through the proposed color representations, where the compressions are being done and what zones are more affected by them. Also, one can easily follow the needle path by analyzing the deformations caused by the needle insertion.

It was observed that the best results for elastography measurements are acquired using values from various video acquisitions, taking the local Young's Moduli that correspond to the higher Coefficients of Determination. Also, between the attempted modes of acquisition and protocols, the best results correspond to ultrasound video data acquired in the Siemens Acuson p500 system, fixing the probe in order to scan the side of the phantom and increasing the weights placed on the phantom from 500 g to 2000 g (protocol 2).

For a homogeneous phantom, the global Young's Modulus resultant from the combination of the best values of different ultrasound videos differs from the reference (compression test in which the distance between phantom surfaces is measured) only by 0.95 kPa.

For a phantom with a small inclusion, in which the softer and stiffer part were analyzed individually, the best result for the stiff inclusion differs in 1.36 kPa from the reference. The best result for the soft part of the phantom is 8.63 kPa higher than the reference.

In the same way, for a phantom in which the stiffer inclusion and soft part could be seen in the same video images, the best results for the stiff inclusion are 1.41 kPa lower than the reference values, but the soft part has a Young's Modulus 11.53 kPa above the reference value.

In a biphasic phantom, the best result for the soft part differs in 5.52 kPa from the reference, and the best result for the stiffer part is only 1.73 kPa higher than the reference.
These results suggest that the calculated Young's Moduli for the softer area in a phantom with a stiff lesion is prone to be overestimated in comparison to the reference, using the proposed methods. The results are summed up in the table on **figure 65**.

| Phantom | Compression test Young's Modulus (kPa) | Best result combination Young's Modulus (kPa) | Error (kPa) (best result combination – compression test result) |
|---|---|---|---|
| Homogeneous | 22.66 | 23.61 | +0.95 |
| Stiff lateral inclusion (1) | 41.75 | 40.39 | -1.36 |
| Soft bulk (1) | 17.81 | 26.44 | +8.63 |
| Stiff centered inclusion (2) | 41.75 | 40.34 | -1.41 |
| Soft bulk (2) | 17.81 | 29.34 | +11.53 |
| Biphasic soft part | 18.21 | 23.73 | +5.52 |
| Biphasic stiff part | 30.03 | 31.76 | +1.73 |

*Figure 65 – summary of the final elastography results for the different phantoms and phantom zones. (1) and (2) correspond to different phantoms: (1) is for the phantom with a small stiff lateral inclusion and (2) for the phantom with a bigger, centered, stiff inclusion.*

The results also confirm that the developed techniques can accurately measure displacements and Young's Moduli in homogeneous phantoms, and that relative stiffness values can be easily observed in heterogeneous phantoms – even though their values may not be as accurately estimated as necessary, one can have the perception of where are the stiffer and softer regions in a phantom through the proposed methodologies.

## VI. Future Work

Because the proposed methodologies require a fixed referential, placed in a phantom, for the displacements to be measured and for the elastography data to be acquired, the future work should aim for the same goal, but gradually removing the necessity for a referential, so that results could be acquired during breast ultrasound procedures, and even during ultrasound-guided biopsies. Moving toward real-time results would be useful for this.

The latter are results to be achieved in a final development of the concepts underlying this project, but there are some less distant, more approachable improvements that should be done in the future: the compression tests done for the creation of a reference in Young's Moduli, for the different phantoms, were done in a simplified way and should be replaced by high precision tests made with compression test machines. The acquired results with simplified compression tests did not allow for a difference to be seen in the Young's Modulus for a phantom with referential lines and without them. This study should be conducted, so that the effects of the presence of referential lines in terms of the stiffness can be analyzed.

Furthermore, the proposed methods for elastography can be, in the future, used as a mean of comparison with other methods for elastic properties estimation, not based on ultrasound imaging, for example.

Also, getting enough granularity on the referential grid to have a higher accuracy prediction on elastic properties should be one of the future goals. Then, one could analyze the following problem: having the elastography data for a phantom, acquired with the proposed techniques, and an elastography color map of a real breast, created by an elastography program, present in some ultrasound machine models, compare the resultant values of elasticity for both methods. When accuracy is high enough, one can use the results in this proposed technique to transfer a "virtual referential" to a real breast case and measure the deformations in the real breast.

## Appendix

The Guided User Interface used in this project was done using Matlab GUIDE Tool (GUI Development Environment). Its use is demonstrated in the images presented in this appendix.

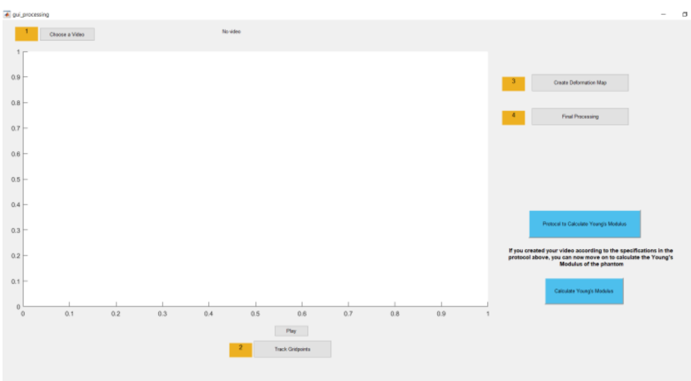

*Figure 1 – running **gui_processing.m**, the user interface should appear and look like this. No video is selected yet.*

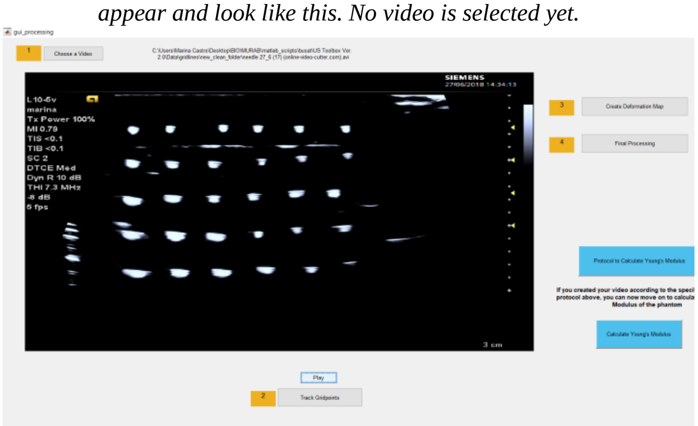

*Figure 2 – after choosing a needle insertion video, on number 1, "choose video", and hitting "Play", the video should be shown in the figure space.*

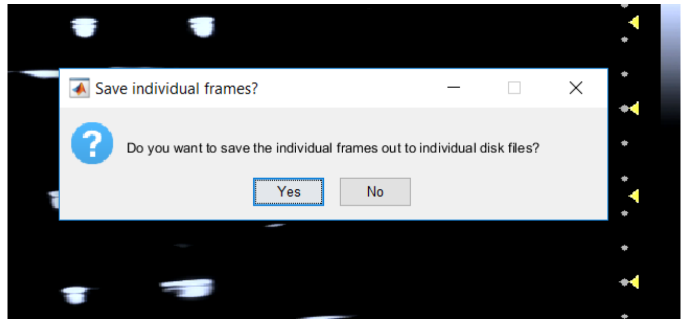


*Figure 3 – clicking on the button 2, "Track Gridpoints", this dialog box appears, asking whether one wants to save the individual frames out to individual disk files or not. One may not want to save the frames out to individual files it was already done before. If so, clicking "No" will command the program to look for the folder where the processed frames may be, for this specific video, and open it, showing the saved processed images.*

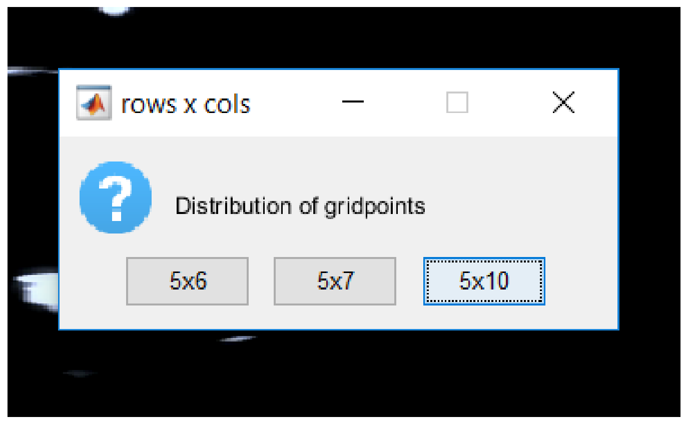


*Figure 4 – clicking "Yes" in the dialog box of figure 3 will open this dialog box. Here, one is asked what is the distribution of gridpoints that is to be visualized. To choose a great distribution of gridpoints, aiming for the inclusion of the bigger number of frames possible in the results, one must visualize the original video and see whether there are lines or columns that get occluded at some time point in the video, and select a number of rows and columns based on the distribution that is more likely to be maintained throughout the whole video, without noise insertion.*

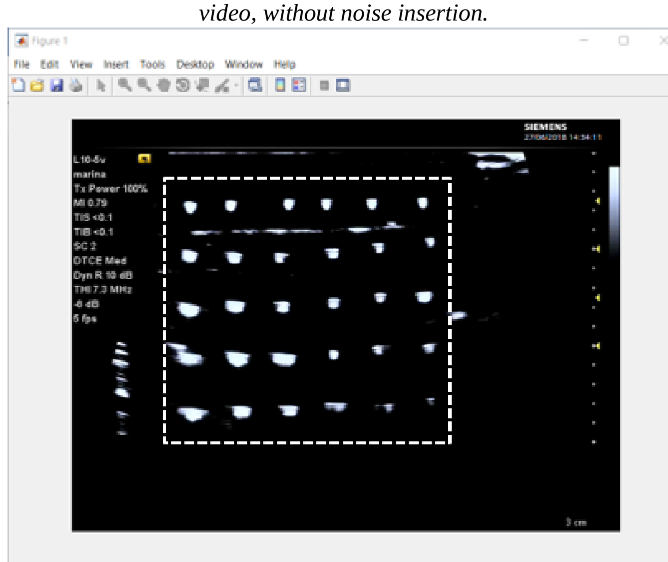


*Figure 5 – selecting a distribution of gridpoints, the user is asked to create a Region of Interest in the first frame of the video. A selection tool is created for this purpose and the user must select as*

*many lines and columns as they have chosen to in the dialog box of figure 4. In this case, the user chose to consider 5 lines and 6 columns.*

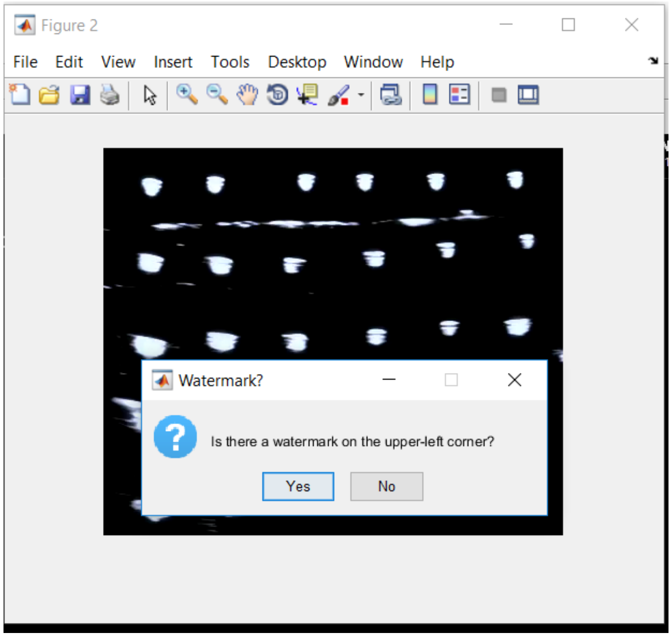


*Figure 6 – when one selects a Region of Interest, a dialog box is shown, asking if there is a watermark in the upper-left corner. This image does not have it.*

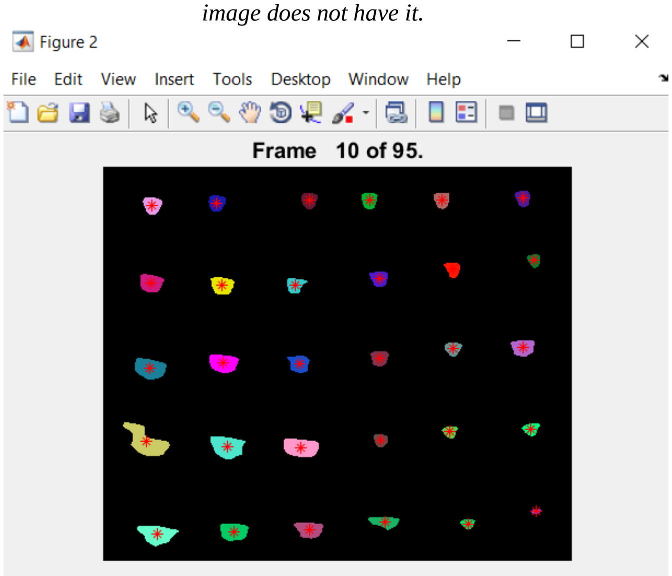


*Figure 7 – After selecting an option in the dialog box of figure 6, the processing starts, and the gridpoints are tracked for each image. In this case, the frame that is being processed and showed is the frame 10 out of a total of 95.*

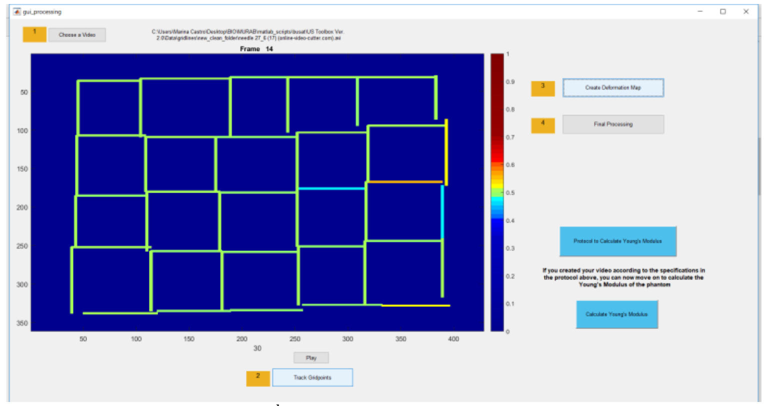

*Figure 8 – Clicking the 3rd button, "Create Deformation Map", the distances between the gridpoints are calculated and color-coded for their representation as a deformation map.*

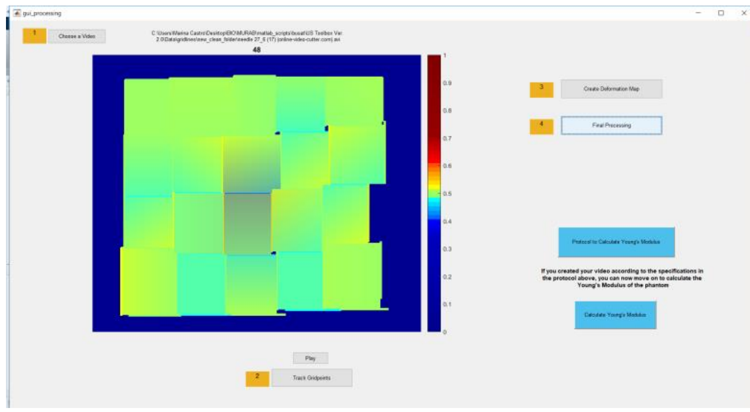

*Figure 9 – Clicking the 4th button, "Final Processing" will generate the color interpolation images for each frame. One should only select this option after the Deformation Map is concluded for every frame, since the deformation maps are the base for the interpolation done on Final Processing.*

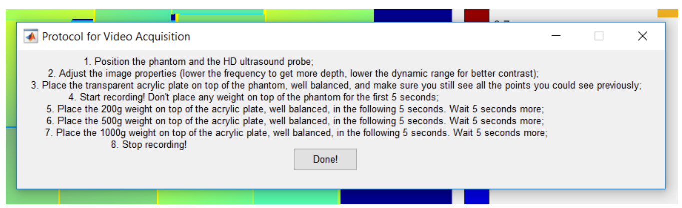


*Figure 10 – clicking on "Protocol to Calculate Young's Modulus", one will see a dialog box with instructions on how to create videos that can be read and processed by the elastography calculation algorithm. Only with these videos the algorithm behind "Calculate Young's Modulus" can proceed.*

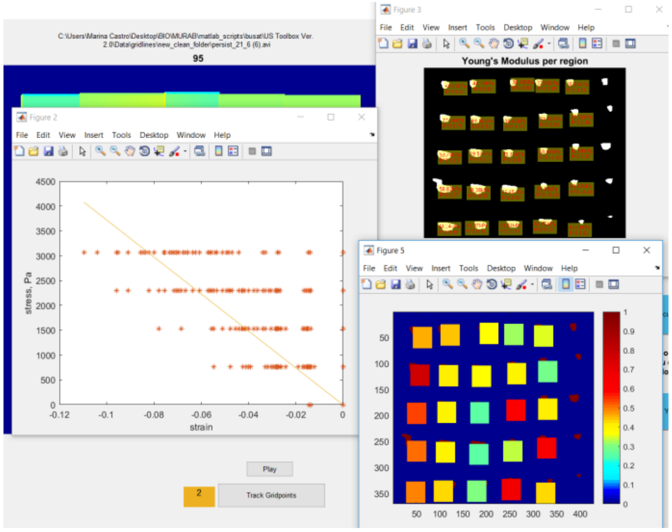


*Figure 11 – clicking "Calculate Young's Modulus" will make the program ask the user to choose a video to process and then make the video go through the same stages shown in figures 3,4,5,6,7 and 8. Then, the local Young's Moduli are calculated, and these presented dialog boxes are shown. The window on the left shows a Stress-Strain plot for all the lines, in all the frames. The window on the upper-right shows the numeric values for the local Young's Moduli, and, under them, the respective Coefficients of Determination. The last image shows a color representation of the Young's Moduli values for each location.*

```
Standard deviation of the Young's moduli: 12.3661
Average R^2: 0.86909
The global Young's Modulus of the phantom is 37.1866 kPa associated to R^2=0.59006
Calculating a weighted average of the local Young's Modulus, leaving out the negative R^2, we get a value of 41.3041 kPa
Used 165 frames to calculate the Young's Modulus
```

*Figure 12 – In the end of this process, the program produces this report, shown in the Command Window.*

## References


[1] T. Greene, C. Cocilovo, A. Estabrook, L. Chinitz, C. Giuliano, S. Rosenbaum Smith e P. I. Tartter, "A Single Institution Review of New Breast Malignancies Identifie Solely by Sonography," *Journal of the American Colleg of Surgeons*, vol. 203, nº 6, pp. 894-898, 1 12 2006.

[2] C. D. Lehman, "Role of MRI in screening women at higl risk for breast cancer," *Journal of Magnetic Resonance Imaging*, vol. 24, nº 5, pp. 964-970, 1 11 2006.

[3] C. H. Lee, D. D. Dershaw, D. Kopans, P. Evans, B. Monsees, D. Monticciolo, R. J. Brenner, L. Bassett, W. Berg, S. Feig, E. Hendrick, E. Mendelson, C. D'Orsi, E. Sickles e L. W. Burhenne, "Breast Cancer Screening Wi Imaging: Recommendations From the Society of Breast Imaging and the ACR on the Use of Mammography, Breast MRI, Breast Ultrasound, and Other Technologies for the Detection of Clinically Occult Breast Cancer," *Journal of the American College of Radiology*, vol. 7, nº pp. 18-27, 1 1 2010.

[4] H. Hille, "Advances in Breast Ultrasound," em *Sonography*, InTech, 2012.

[5] T. M. Kolb, J. Lichy e J. H. Newhouse, "Comparison of the Performance of Screening Mammography, Physical Examination, and Breast US and Evaluation of Factors that Influence Them: An Analysis of 27,825 Patient Evaluations," *Radiology*, vol. 225, nº 1, pp. 165-175, 10 2002.

[6] N. Houssami, L. Irwig, J. M. Simpson, M. McKessar, S. Blome e J. Noakes, "<b>Sydney Breast Imaging Accuracy Study:</b> Comparative Sensitivity and Specificity of Mammography and Sonography in Young Women with Symptoms," *American Journal of Roentgenology*, vol. 180, nº 4, pp. 935-940, 23 4 2003.

[7] W. A. Berg, "Rationale for a Trial of Screening Breast Ultrasound: American College of Radiology Imaging Network (ACRIN) 6666," *American Journal of Roentgenology*, vol. 180, nº 5, pp. 1225-1228, 23 5 2003.

[8] P. Busilacchi, F. Draghi, L. Preda e C. Ferranti, "Has color Doppler a role in the evaluation of mammary lesions?," *Journal of Ultrasound*, vol. 15, nº 2, pp. 93-98, 1 6 2012.

[9] Guofang Xiao, J. Brady, J. Noble, M. Burcher e R. English, "Nonrigid registration of 3-D free-hand ultrasound images of the breast," *IEEE Transactions on Medical Imaging*, vol. 21, nº 4, pp. 405-412, 4 2002.

[10] J. Bonnema, A. N. v. Geel, B. v. Ooijen, S. P. Mali, S. L. Tjiam, S. C. Henzen-Logmans, P. I. Schmitz e T. Wiggers, "Ultrasound-Guided Aspiration Biopsy for Detection of Nonpalpable Axillary Node Metastases in Breast Cancer Patients: New Diagnostic Method," *World Journal of Surgery*, vol. 21, nº 3, pp. 270-274, 1 3 1997.

[11] B. Maris, F. Visentin and V. Groenhuis, "Review on non-rigid local deformation models in 3D medical images," 2017.

[12] S. PANDYA e R. G. MOORE, "Breast Development and Anatomy," *Clinical Obstetrics and Gynecology*, vol. 54, nº 1, pp. 91-95, 3 2011.

[13] M. Hamdi, E. Würinger, I. Schlenz e R. Kuzbari, "Anatomy of the Breast: A Clinical Application," em *Vertical Scar Mammaplasty*, Berlin, Heidelberg, Springer Berlin Heidelberg, 2018, pp. 3-12.

[14] Y. Payan, J. Ohayon e M. Nash, Biomechanics of Living Organs Hyperelastic Constitutive Laws for Finite Element Modeling., Academic Pr, 2017.

[15] R. A. Jesinger, "Breast anatomy for the interventionalist.," *Techniques in vascular and interventional radiology*, vol. 17, nº 1, pp. 3-9, 1 3 2014.

[16] D. T. Ramsay, J. C. Kent, R. A. Hartmann e P. E. Hartmann, "Anatomy of the lactating human breast redefined with ultrasound imaging," *Journal of Anatomy*, vol. 206, nº 6, pp. 525-534, 1 6 2005.

[17] B. A. Howard e B. A. Gusterson, "Human Breast Development," *Journal of Mammary Gland Biology and Neoplasia*, vol. 5, nº 2, pp. 119-137, 2000.

[18] T. Rohlfing, C. Maurer, D. Bluemke e M. Jacobs, "Volume-preserving nonrigid registration of MR breast images using free-form deformation with an incompressibility constraint," *IEEE Transactions on Medical Imaging*, vol. 22, nº 6, pp. 730-741, 6 2003.

[19] P. R. Bakic, M. Albert, D. Brzakovic e A. D. A. Maidment, “Mammogram synthesis using a 3D simulation. I. Breast tissue model and image acquisition simulation,” *Medical Physics,* vol. 29, nº 9, pp. 2131-2139, 27 8 2002.

[20] F. S. Azar, D. N. Metaxas e M. D. Schnall, “A deformable finite element model of the breast for predicting mechanical deformations under external perturbations.,” *Academic radiology,* vol. 8, nº 10, pp. 965-75, 1 10 2001.

[21] S. DiMaio e S. Salcudean, “Needle insertion modeling and simulation,” *IEEE Transactions on Robotics and Automation,* vol. 19, nº 5, pp. 864-875, 10 2003.

[22] G.-F. W. d. A.-P. W. Rodríguez-Cristerna A., “BUSAT: A MATLAB Toolbox for Breast Ultrasound Image Analysis,” em *Carrasco-Ochoa J., Martínez-Trinidad J., Olvera-López J. (eds) Pattern Recognition. MCPR 2017. Lecture Notes in Computer Science, vol 10267. Springer, Cham*, 2017.

[23] P. B. Gordon e S. L. Goldenberg, “Malignant breast masses detected only by ultrasound. A retrospective review,” *Cancer,* vol. 76, nº 4, pp. 626-630, 15 8 1995.

[24] I. Embryology, “Anatomy of the Human Body Henry Gray CONTENTS”.

## Thank You Note

To Vincent Groenhuis, Msc., for the ideas, patience and all the help and encouragement; to Rianne van Dommelen, Bsc., and her team from BMPI (Biomedical Photonic Imaging) for the insights on PVC phantom production methods; to Marcel Schwirtz, ing., Henny Kuipers and Sander Smits, ing., for all the help in the lab; to MD Jeroen Veltman, radiologist in ZGT Hengelo, for showing me ultrasound, ultrasound-guided biopsy and MRI-guided biopsy procedures in the breast, and providing with the user stories necessary for the further development of this project; to Jolanda Boelema-Kaufmann for all the help and for caring so much about her “RAM kids”; finally to Prof. Dr. Stefano Stramigioli, Dr. Françoise Siepel and Vincent Groenhuis, Msc., for the opportunity of doing this project in this amazing place.